https://doi.org/10.1016/j.surfcoat.2020.125919

Comparison of corrosion resistance and biocompatibility of magnesium phosphate (MgP), zinc phosphate (ZnP) and calcium phosphate (CaP) conversion coatings on Mg alloy

WeiZai[a] Xiaoru Zhang[a] Yingchao Su[b] H.C. Man[c] Guangyu Li[a]J ianshe Lian[a]

Abstract

Seven different conversion coatings (which can be classified into three types: MgP, ZnP and CaP) were prepared on Mg alloy substrates to compare the corrosion resistance and biocompatibility of these coatings. Biocompatibility and cytotoxicity of different coated samples and bare Mg alloy were studied using the CCK-8 test. The corrosion resistance of different conversion coatings was comparatively studied by electrochemical tests (OCP, EIS and PDP) and long-term immersion test in Hanks' solution. Based on the experimental results, the corrosion mechanism of different types of conversion coatings and Mg alloy substrate was proposed and investigated.

Keywords

Phosphate conversion coating; Magnesium alloy; Corrosion resistance; Electrochemical measurements; Hydrogen evolution; Biocompatibility

1. Introduction

As promising biodegradable materials, magnesium (Mg) and its alloy have attracted the attention of numerous researchers due to their excellent cell biocompatibility [[1], [2], [3], [4]] and good biomechanical compatibility [[5], [6], [7], [8]]. Furthermore, the biodegradable nature of Mg alloys makes them a desirable candidate for orthopedic implants in bone fracture surgery in contrast to permanent implants made [[9], [10], [11], [12], [13]] when bone healing is completed [14].

However, the high corrosion rate of Mg alloys hinders their immediate applications as biodegradable implants. The rapid dissolution of Mg alloys in body fluids results in a series of problems such as excessive hydrogen evolution, alkalization of the tissue microenvironment and inadequate mechanical strength of the implant or even premature failure [15]. Thus the most important issue to address in the development of Mg implants is the improvement in corrosion resistance.

A considerable effort has been devoted to improving the corrosion resistance of Mg-based materials, including composition adjustment and surface modification. In this connection, a wide spectrum of techniques has been attempted. Micro-arc oxidation (MAO) [16,17], sol-gel coating [18], physical vapor deposition (PVD) [19,20], chemical vapor deposition (CVD) [21], polymer coating [15] and chemical conversion coatings [[22], [23], [24]] have been reported in the literature as attempts to enhance the corrosion performance of Mg-based materials. Among these techniques, chemical conversion coating, being a simple wet chemical method, can effectively form uniform coating despite the irregular shape of the substrate. In the past decade, phosphate coatings formed by chemical conversion has been employed to improve the anti-corrosion performance of Mg-based biomaterials, including such as magnesium phosphate (MgP) [25,26], calcium phosphate (CaP) [[27], [28], [29]] and zinc phosphate (ZnP) [30,31]. However, the corrosion behavior, (both short term and long-term) and biocompatibility of these phosphate conversion coatings have not been thoroughly studied and compared.

In this work, seven kinds of conversion coatings (Mg-P, Zn-P, Ca-P, ZnMg-P, CaMg-P, ZnCa-P and ZnCaMg-P) were prepared using different conversion coating solutions. The morphologies, corrosion behavior, biocompatibility of these conversion coatings were compared and discussed

2. Experimental procedure

2.1. Materials and preparation

Wrought AZ31 Mg alloy with a composition of 3.1 wt% Al, 0.9 wt% Zn, 0.1 wt% Mn and Mg balance was cut into rectangular plates of dimensions 15 × 15 × 2 mm. Before the conversion coating procedure, the substrate was polished using sandpaper from grade 360 to 2000 and ultrasonically cleaned in acetone for about 3 min to remove contaminants. To investigate the influence of Mg^{2+}, Zn^{2+} and Ca^{2+} ions on phosphate conversion coatings, seven kinds of phosphate conversion coatings were prepared in different solutions with a pH of 2.7 at 60 °C for

20 min. The specific compositions of these conversion coating solutions are presented in Table 1. The amounts of Mg^{2+}, Zn^{2+} and Ca^{2+} ions were determined according to the predominance area diagrams shown in Fig. 16 with a pH of 2.7.

Table 1. Compositions of phosphate conversion coating solutions with a pH of 2.7.

Samples	**Chemical composition (mol/L)**					
	$Mg(NO_3)_2$	**$Zn(NO_3)_2$**	**$Ca(NO_3)_2$**	**H_3PO_4**	**NaOH**	**H_2O**
Mg-P	0.4	–	–	0.2	Bal.	Bal.
Zn-P	–	0.1	–	0.2	Bal.	Bal.
Ca-P	–	–	0.2	0.2	Bal.	Bal.
ZnMg-P	0.4	0.1	–	0.2	Bal.	Bal.
CaMg-P	0.4	–	0.2	0.2	Bal.	Bal.
ZnCa-P	–	0.1	0.2	0.2	Bal.	Bal.
ZnCaMg-P	0.4	0.1	0.2	0.2	Bal.	Bal.

2.2. Thermodynamic calculations

Predominance area diagram as a common basis for the design of conversion coatings [22,26,[32], [33], [34], [35]] was calculated using MEDUSA software (Make Equilibrium Diagrams Using Sophisticated Algorithms) according to the database HYDRA (Hydrochemical Equilibrium Constant Database) in this work. Predominance area diagrams of magnesium phosphates, zinc phosphates and calcium phosphates were calculated with a constant concentration (0.2 mol/L) of phosphate at room temperature (25 °C).

2.3. Microstructural characterization and compositional analysis

Surface morphologies, cross-section morphologies and chemical compositions of different samples were obtained using a scanning electron microscope (SEM, Tescan VEGA3) equipped

with an energy-dispersive spectrometer (EDS, Oxford Instrument). The phase composition of coated samples was investigated using X-ray diffraction (XRD, Rigaku Dymax, Japan) with Cu Kα ($\lambda = 0.154178$ nm) radiation at 20 mA and 40 kV. The scanning angle (2θ) of XRD measurement was set from 10° to 60°, with a scanning rate of 4°/min.

2.4. Mechanical properties

The adhesive strength of coated samples was investigated using a standard tensile adhesion test (ASTM C 633 [36]) by a universal testing system (MTS 810, USA) at a constant speed of 0.01 mm/s and 4 replicates were tested to ensure reliability. The counter pull-off bar with an area of 1.0 cm^2 was roughened by 60-grade sandpaper and then adhered to the surface of coated samples with epoxy resin (3 M DP420 epoxy adhesive).

2.5. Cell viability test

The Cell Counting Kit-8 (CCK-8) assays were performed to evaluate the biocompatibility of bare AZ31 Mg alloy and all coated samples. 100 μL cell suspensions (MC3T3-E1) with a density of 2000 cells/well were seeded in a 96-well plate for 24 h and then co-cultured with the extracts which were prepared from all samples according to ISO 10993-5 [37], and three replicates were conducted for each sample. After co-culturing for 1, 3 and 5 days, 10 μL CCK-8 solution was added to each well and incubated for 2 h, and then the optical density (*OD*) of each well was measured and recorded with a microplate reader (Tecan F50) at 450 nm. The cell viability was expressed by the cell relative growth rate (*RGR*) according to the following expression (Eq. (1)).(1)RGR=ODtest/ODnegtive×100%

2.6. Electrochemical tests

Short-term electrochemical tests, including open-circuit potential (OCP) test and potentiodynamic polarization (PDP) test, were carried out in Hanks' solution with a pH value of 7.4 and at 37 °C using an electrochemical station (STAT3, Princeton Applied Research, USA) in a traditional three-electrode cell. A platinum plate with an area of 1 cm^2, a saturated calomel electrode (SCE) and the sample with an exposed area of 1 cm^2 served as the counter electrode (CE), reference electrode (RE) and working electrode (WE). The composition of Hanks' solution is listed in Table 2 [38]. To ensure steady-state of WE, a short-term OCP test

was carried out for 20 min before the PDP test. After the OCP test, PDP measurement was performed from −200 mV (vs. OCP of each sample) in the anodic direction at a rate of 1 mV/s.

Table 2. Composition of Hanks' solution [38].

Chemical	NaCl	KCl	$NaHCO_3$	$MgSO_4 \cdot 7H_2O$	Glucose	$CaCl_2$	KH_2PO_4	$Na_2HPO_4 \cdot 2H_2O$
Mass (g/L)	8	0.4	0.35	0.2	1	0.14	0.06	0.06

2.7. Immersion test

To evaluate the degradation properties of coated samples, in vitro degradation immersion test was carried out in Hanks' solution with a pH of 7.4 at 37 °C for 15 days. All samples with an exposed area of 2 cm^2 were immersed in 300 mL of Hanks' solution. Hydrogen evolution volumes were collected by a burette and recorded every day. After the immersion test, macro-morphologies and micro-morphologies of all samples using optical microscopy (OM) and SEM, and the compositions of corrosion products on their surfaces were analyzed using EDS simultaneously. Electrochemical impedance spectroscopy (EIS) test was conducted to detect the corrosion state change of all samples during the long-term immersion test. EIS test was run from 100 kHz to 0.01 Hz with an AC amplitude of 10 mV (vs. OCP) and the test result was fitted by ZSimpWin software. Meanwhile, long-term OCP measurement of all samples was conducted.

3. Results

3.1. Coating characterization

The XRD patterns of seven kinds of conversion coatings are shown in Fig. 1. The main phase of Mg P is newberyite ($MgHPO_4 \cdot 3H_2O$) while Zn P, ZnMg-P, ZnCa-P and ZnCaMg-P have the same main phase of zinc phosphate hydrate ($Zn_3(PO_4)_2 \cdot 4H_2O$), but their crystallinity and grain orientation differ. ZnCa-P coating has the highest crystallinity and Zn P has the lowest crystallinity. Ca P and CaMg-P have similar patterns and their main phase is dicalcium phosphate dehydrate ($CaHPO_4 \cdot 2H_2O$, DCPD). According to the main phases of different conversion coatings, these seven conversion coatings are classified into three types:

MgP type (only Mg P), ZnP type (including Zn P, ZnMg-P, ZnCa-P and ZnCaMg-P) and CaP type (including Ca P and CaMg-P).

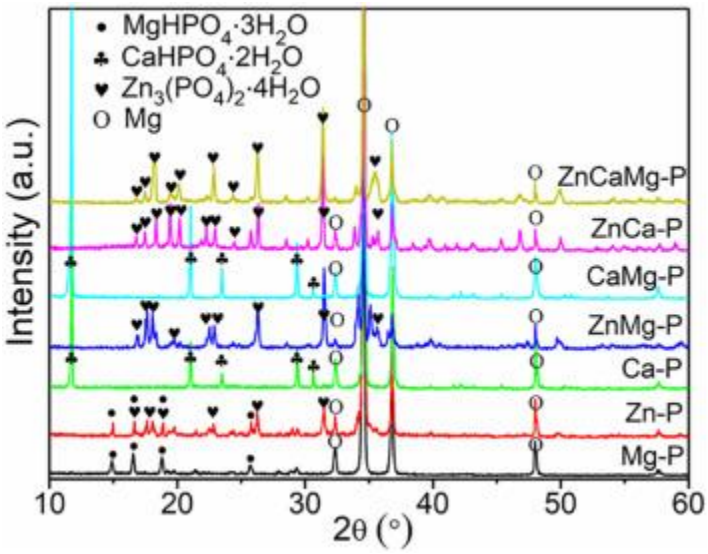

Fig. 1. The XRD patterns of seven kinds of conversion coatings.

The SEM surface morphologies of all conversion coatings and bare AZ31 Mg alloy substrate are presented in Fig. 2 and the corresponding EDS result of all conversion coatings are presented in Fig. 3. Mg-P coating (Fig. 2(a)) consists of cubes with an average dimension of 5 μm. According to the XRD and EDS results as shown in Fig. 1 and Fig. 3(a), it can be concluded that the main phase of Mg-P coating is newberyite $MgHPO_4 \cdot 3H_2O$. As shown in the SEM morphologies (Fig. 2(c) and (e)), Ca-P coating consists of lath-like crystals, and CaMg-P coating consists of flake-like crystals erected on the substrate. The elemental compositions (shown in Fig. 3(c) and (e)) of CaP and CaMg-P coatings are similar and the EDS results are consistent with the XRD patterns of $CaHPO_4 \cdot 2H_2O$ (DCPD). According to the EDS results in Fig. 3(b)(d)(f)(g) and XRD patterns, the ZnP type conversion coatings Zn-P, ZnMg-P, CaZn-P and ZnCaMg-P all contain ($Zn_3(PO_4)_2 \cdot 4H_2O$) as the main phase, though these four coatings show different appearances. Zn-P coating consists of flakes, ZnCa-P coating consists of thin sheets, whereas ZnMg-P and ZnCaMg-P coating are composed of particle-like aggregates which are stacked by dense layers.

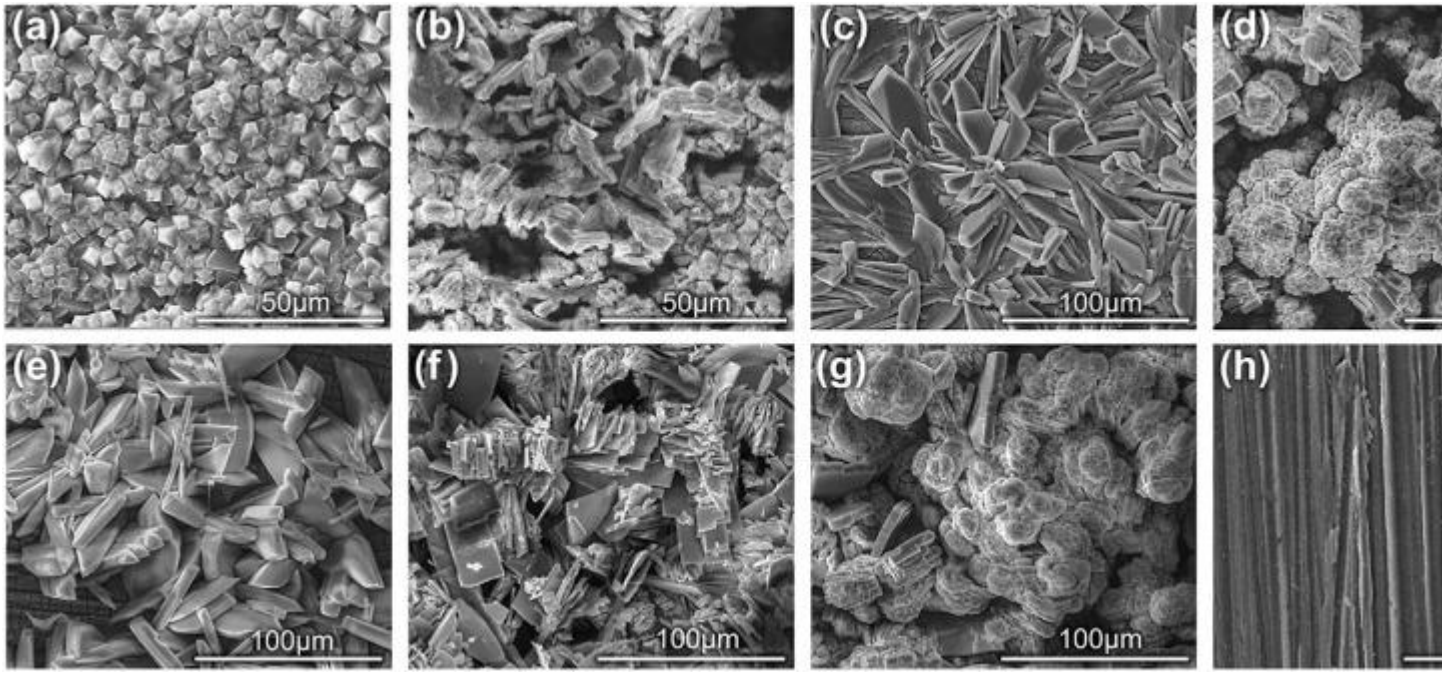

Fig. 2. SEM surface morphologies of coated samples: (a) Mg P, (b)Zn-P, (c) Ca P, (d) ZnMg-P, (e) CaMg-P, (f) ZnCa-P, (g) ZnCaMg-P and (h) bare substrate of AZ31 Mg alloy.

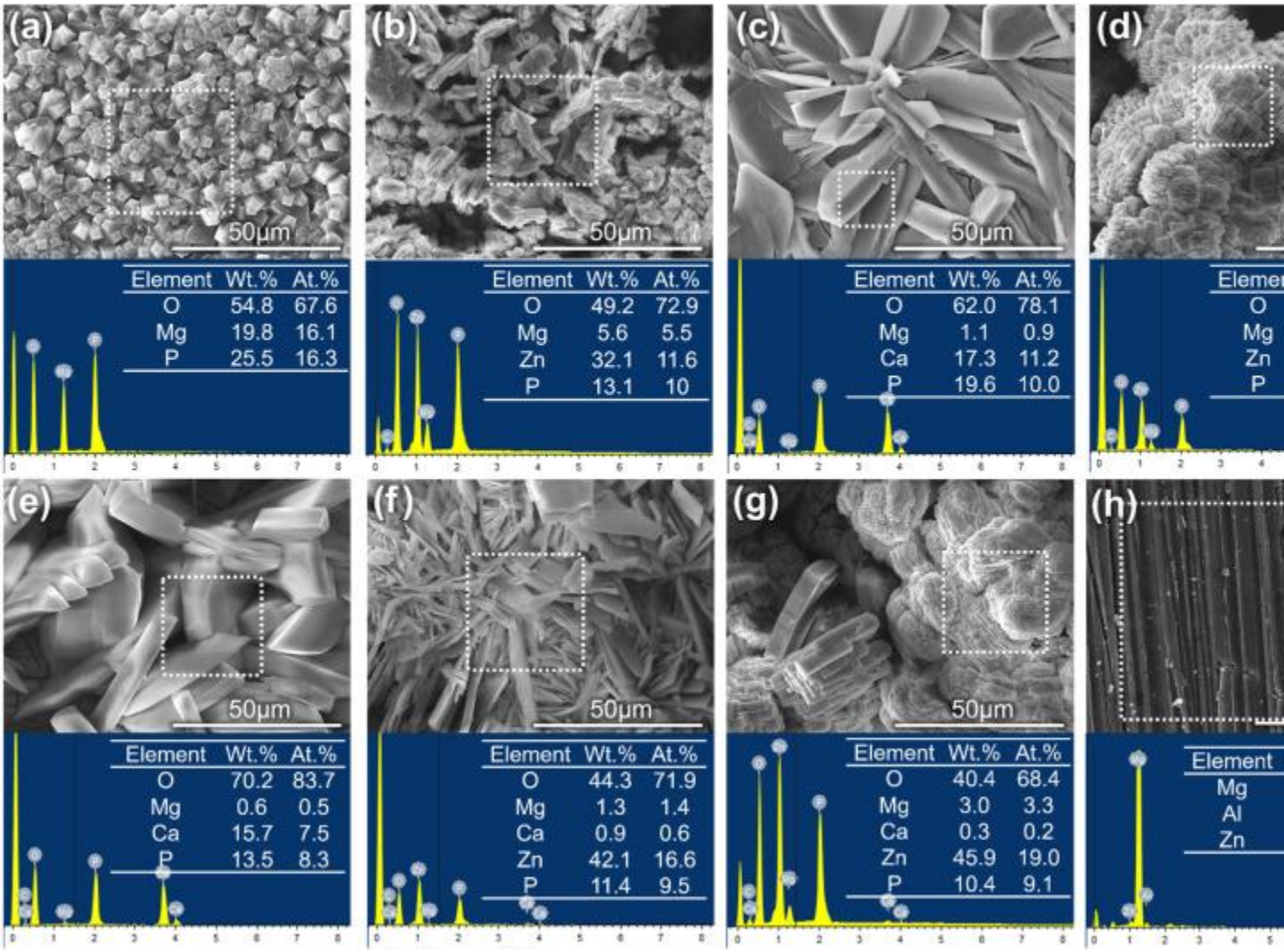

Fig. 3. EDS results and corresponding tested area of coated samples: (a) Mg P, (b) Zn-P, (c) Ca-P, (d) ZnMg-P, (e) CaMg-P, (f) ZnCa-P (g) ZnCaMg-P and (h) bare substrate of AZ31 Mg alloy.

Fig. 4 shows the OM surface morphologies of all coated samples and bare substrate AZ31 Mg alloy. Mg-P, Zn-P, Ca-P and CaMg-P coating are more uniform than other coatings. With the addition of Mg^{2+} or Ca^{2+} ions in Zn-P conversion solution (Table 1), ZnMg-P and ZnCa-P coatings convert from white (Fig. 4(b)) to gray. Once Mg^{2+} and Ca^{2+} ions are added into conversion solution (Table 1), ZnCaMg-P coating appears obviously blacker, and the contention of element Zn in ZnCaMg-P coating is more than that in ZnMg-P coating which is probably caused by the metallic Zn formed in that coating.

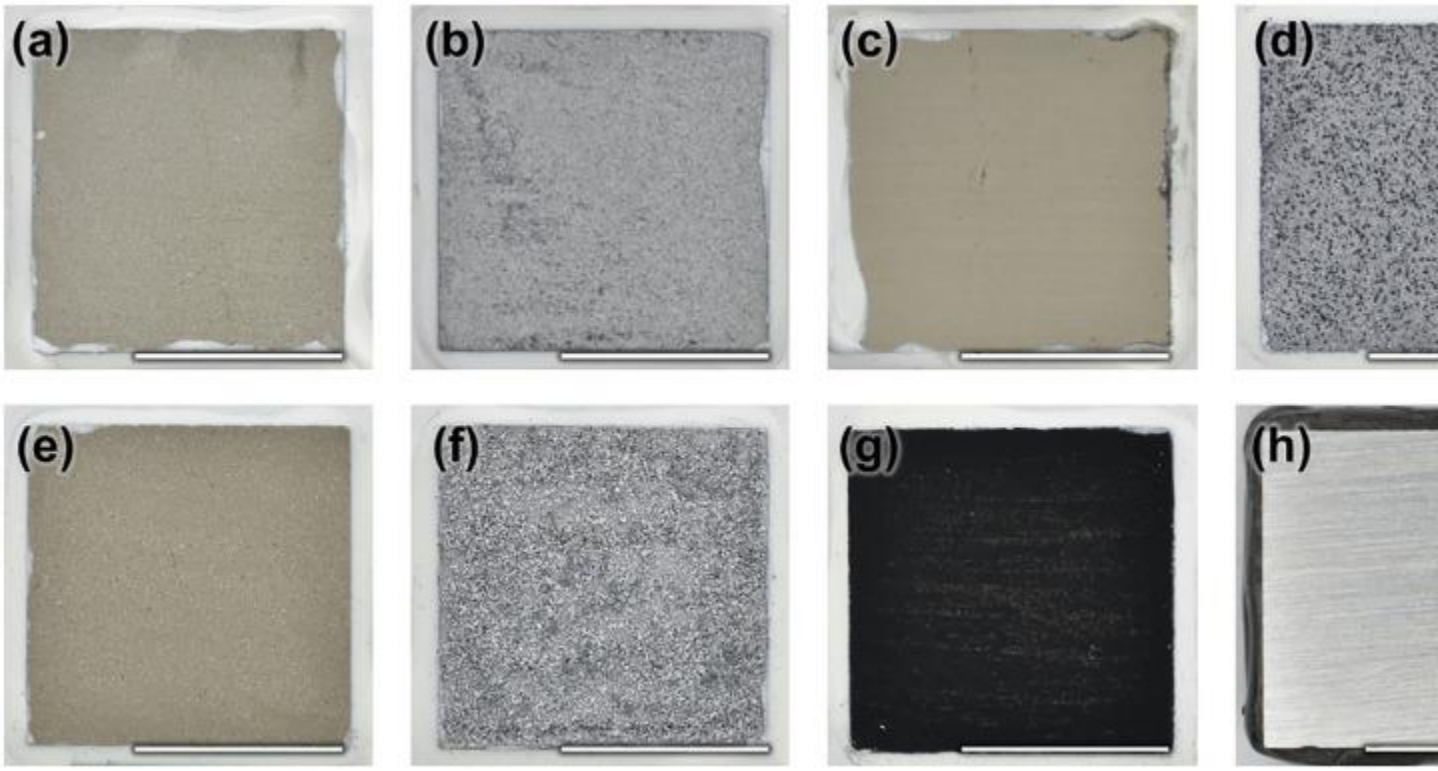

Fig. 4. OM surface morphologies of coated samples: (a) Mg P, (b) Zn P, (c) Ca P, (d) ZnMg-P, (e) CaMg-P, (f) ZnCa-P, (g) ZnCaMg-P and (h) bare substrate of AZ31 Mg alloy (the scales bar is 10 mm).

Fig. 5 shows the cross-section morphologies of all coated samples. Mg-P and Ca-P coatings are relatively thin, about 17 and 15 μm. Coating ZnCa-P has a maximum thickness of up to 125 μm. The thickness values of coating Zn-P, ZnMg-P, CaMg-P and ZnCaMg-P are about 55, 55, 40 and 73 μm, respectively.

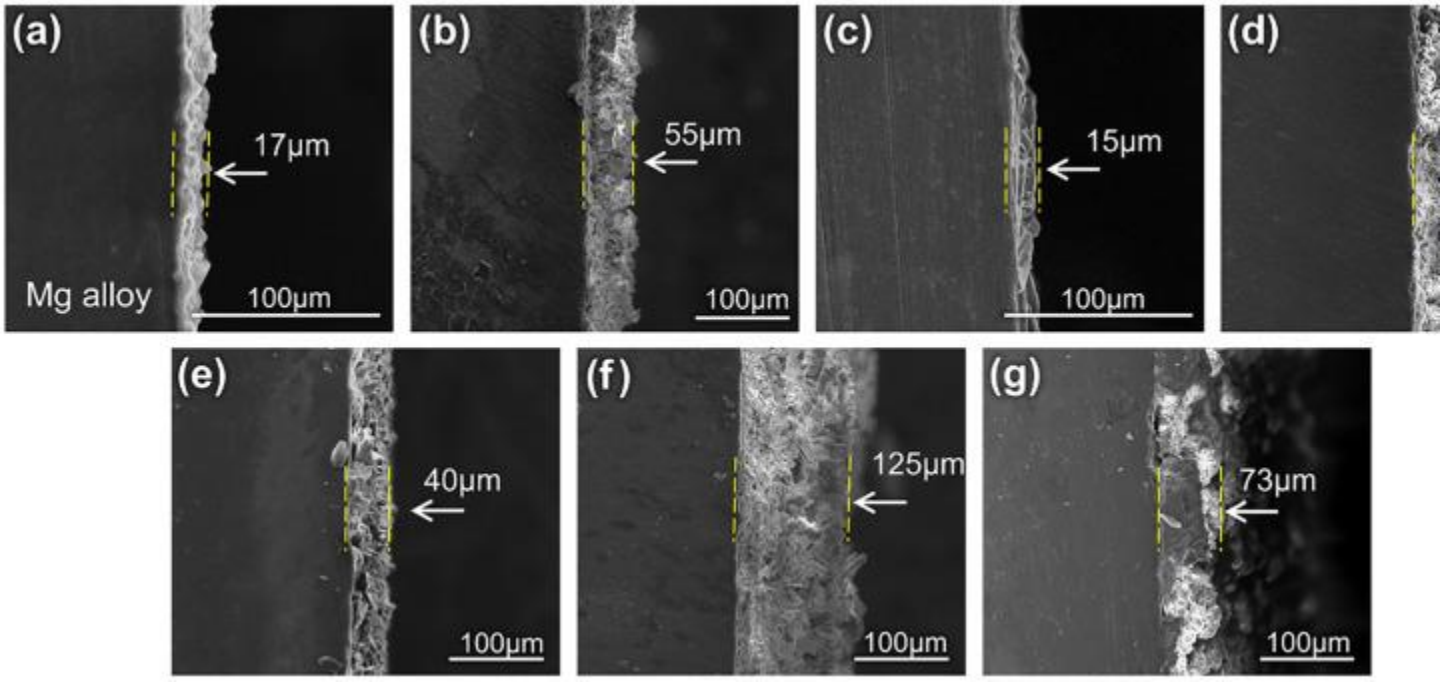

Fig. 5. Cross-section morphologies of coated samples: (a) Mg P, (b) Zn P, (c) Ca P, (d) ZnMg-P, (e) CaMg-P, (f) ZnCa-P and (g) ZnCaMg-P.

3.2. Mechanical property

Fig. 6 shows the test result of adhesive strength of all conversion coatings on Mg alloy substrates. Compared with other coatings, coating Mg-P and Ca-P have high adhesive strength, up to 9.4 ± 1.1 and 7.8 ± 1.5 MPa, relatively. ZnMg-P, ZnCaMg-P and CaMg-P coatings have similar adhesive strength of 5.6 ± 1.2, 6.3 ± 0.7 and 5.2 ± 1.3 MPa. Whereas Zn P and ZnCa-P coatings have relatively low adhesive strength of 1.8 ± 0.6 and 2.5 ± 1.3 MPa, which is probably caused by their loose structures. In general, the thin and dense coatings have high adhesive performance, such as the Mg-P and Ca-P coatings.

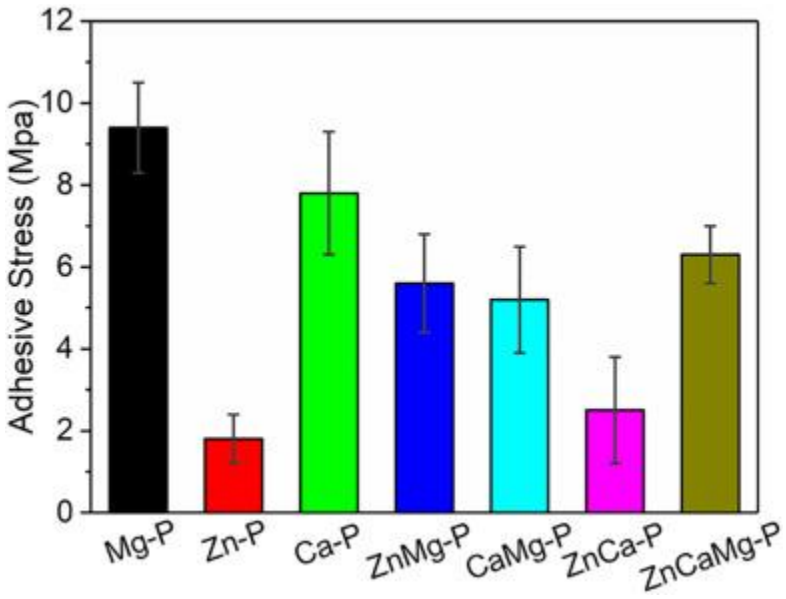

Fig. 6. The adhesive strength of different conversion coatings on the Mg alloy substrate.

3.3. Cell viability test

Fig. 7 shows the result of the indirect contact cell viability test. Compared with coated samples, bare AZ31 Mg alloy has the lowest *RGR*s, which are only about 49%, 36% and 58% on day 1, day 2 and day 5. The *RGR*s of Mg-P coating are about 52%, 43% and 65% on day 1, day 2 and day 5, which are a little higher than that of bare Mg alloy. The ZnP type conversion coatings (Zn-P, ZnMg-P, ZnCa-P and ZnCaMg-P) have similar *RGR*s, which may be caused by their similar composition and corrosion resistance, while the CaP type conversion coatings (Ca-P and CaMg-P) have obviously higher *RGR*s, which are close to the *RGR* of the control, and even up to about 102% and 101% on day 5.

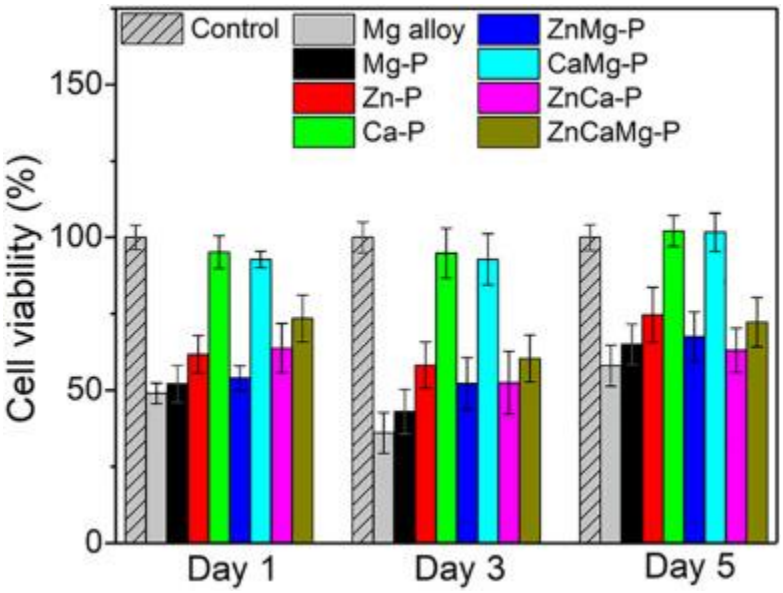

Fig. 7. Cell viability of all coated samples and bare AZ31 Mg alloy after 1, 3 and 5 days of incubation.

3.4. Short-term electrochemical measurements

The short-term OCP curves of coated samples and bare AZ31 Mg alloy tested in Hanks' solution at 37 °C are presented in Fig. 8(a). The OCP curves of Mg-P, Ca-P and CaMg-P are evidently lower than that of the other samples, and the OCP of CaMg-P is the lowest. The probable reason for that low OCP is that dense coating restrains the cathodic reaction on the cathodic phases more than the anodic reaction of Mg substrate and the positive ions have enough time to diffuse. Therefore the OCP decreases in the cathodic direction [22]. In the other OCP curves, Zn-P is close to bare AZ31 Mg alloy, while the OCP curves of the other ZnP type coatings (including ZnMg-P, ZnCa-P and ZnCaMg-P) are relatively higher.

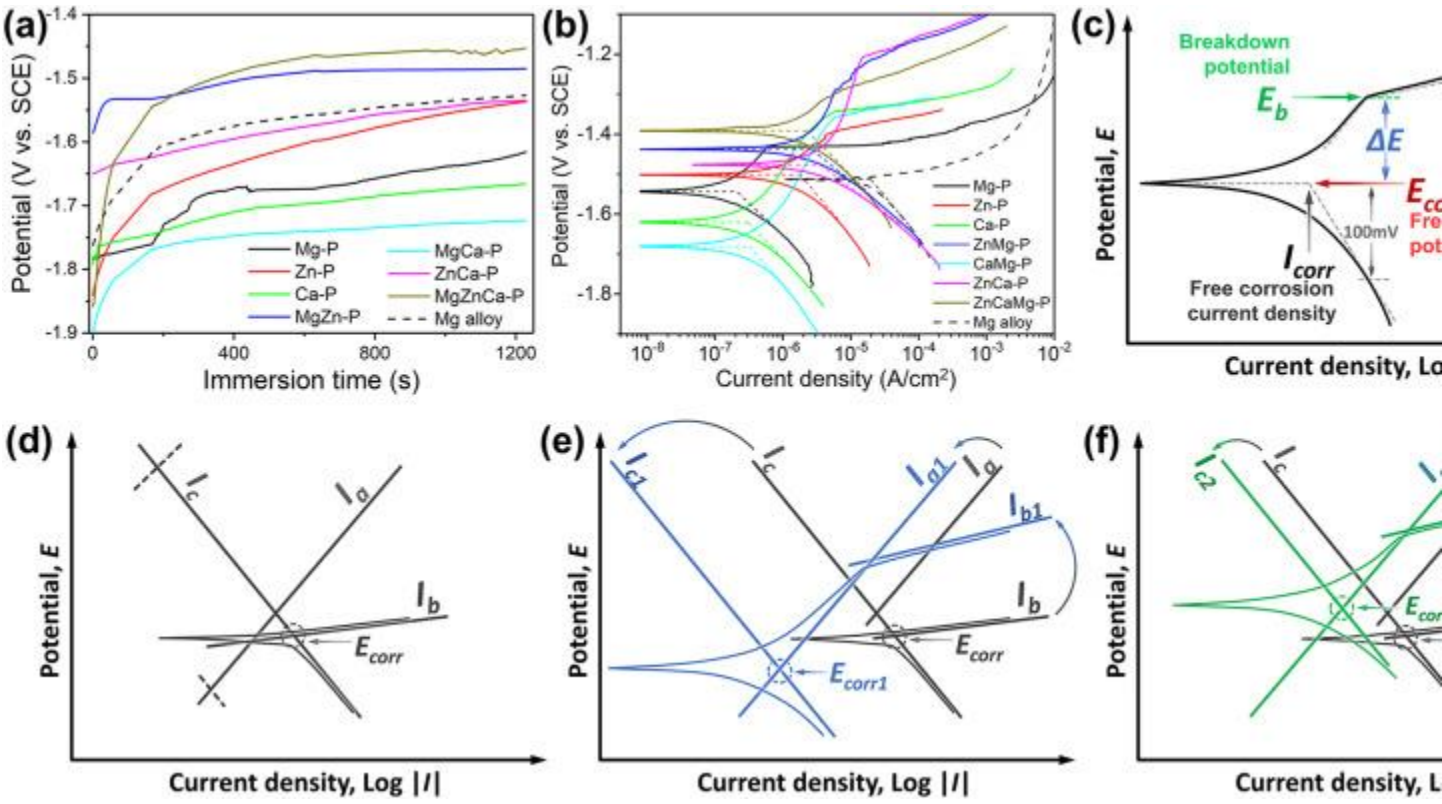

Fig. 8. (a) OCP and (b) PDP curves of coated samples and bare AZ31 Mg alloy tested in Hanks' solution at 37 °C. (c) Schematic diagram of the PDP curve. And schematic polarization diagrams of (d) bare Mg alloy substrate, (e) samples of MgP (Mg P), CaP (Ca-P and CaMg-P) type coatings and (f) samples of ZnP (ZnMg-P, ZnCa-P and ZnCaMg-P) type coatings.

Fig. 8(b) shows the PDP curves of coated samples and bare AZ31 Mg alloy obtained after the short-term OCP measurement, and the corrosion parameters (as depicted in Fig. 8(c)) extracted from the PDP curves are presented in Table 3. The free corrosion potential (E_{corr}) of each sample in Fig. 8(b) has a good correspondence with the OCP curves in Fig. 8(a). Compared with the other coated samples and bare Mg alloy, MgP, Ca-P and CaMg-P have evidently lower free corrosion current densities (i_{corr}), which are 0.206, 0.301 and 0.311 μA/cm^2 respectively. While the coated samples Zn-P, ZnMg-P, ZnCa-P and ZnCaMg-P have relatively larger current densities, with values 1.79, 2.57, 3.54 and 2.19 μA/cm^2 respectively. Compared with all coated samples, bare AZ31 has the largest current density, up to 18.8 μA/cm^2. Since the anodic hydrogen evolution (AHE) and negative difference effect (NDE) phenomenon exist [39],

Mg alloy may rapidly corrode in the anodic region and the breakdown potential of rapid corrosion is defined as E_b. The ΔE ($\Delta E = E_b - E_{corr}$) of coated samples and bare AZ31 the following order: AZ31 (0 V) < ZnCaMg-P (0.085 V) < Zn-P (0.100 V) < Mg-P (0.114 V) < ZnMg-P (0.170 V) < ZnCa-P (0.271 V) < Ca-P (0.280 V) < CaMg-P (0.321 V).

Table 3. Corrosion parameters extracted from the PDP curves shown in Fig. 8(b).

Empty Cell	**Mg alloy**	**Mg-P**	**Zn-P**	**Ca-P**	**ZnMg-P**	**CaMg-P**	**ZnCa-P**	**ZnCaMg-P**
b_a (mV/dec)	–	189	186	250	301	225	318	162
$-b_c$ (mV/dec)	212	165	201	178	146	189	132	171
i_{corr} (μA/cm2)	18.8	0.206	1.79	0.301	2.57	0.311	3.54	2.19
E_{corr} (V vs.SCE)	−1.513	−1.544	−1.502	−1.620	−1.438	−1.681	−1.477	−1.390
E_b (V vs.SCE)	−1.513	−1.430	−1.402	−1.340	−1.268	−1.360	−1.206	−1.305
ΔE (V)	0	0.114	0.100	0.280	0.170	0.321	0.271	0.085

To interpret the polarization behaviors of different samples, schematic polarization diagrams are presented in Fig. 8(d)(e)(f). For the polarization of bare Mg alloy, anomalously low anodic Tafel slope appears on the anodic branch as shown in Fig. 8(b), which corresponds to serious anodic corrosion. Fig. 8(d) shows the polarization diagram of bare Mg alloy substrate, in which lines of I_c and I_a correspond to the currents of cathodic and anodic reactions of bare Mg alloy, whereas I_a can't explain the breakdown anodic reaction. Therefore an extra anodic reaction line (I_b) is postulated to describe the stage of breakdown anodic reaction of bare Mg alloy, which is not strict enough but useful to describe its polarization behavior [40]. Because of the protection of coatings on Mg alloy substrate, MgP (Mg-P), CaP (Ca-P and CaMg-P) type coatings decrease the currents of cathodic and anodic to I_{c1} and I_{a1}, improve the original potential of I_b to I_{b1}, and decrease the free corrosion potential from E_{corr} to E_{corr1}, as shown in Fig. 8(e). Compared with

the decrease of cathodic current of MgP and CaP type coatings (I_{c1}, in Fig. 8(e)), the decrease of cathodic current of ZnP type coatings (I_{c2}, in Fig. 8(f)) is slighter, because the byproduct Zn in the coatings accelerates the cathodic reaction. Therefore the free corrosion potential (E_{corr2}) of ZnP type coatings is higher than that of the Mg alloy substrate(E_{corr1}).

3.5. Long-term immersion test

During the immersion test, the OCP values of bare AZ31 Mg alloy and coated samples were recorded continuously and the results are presented in Fig. 9. Compared with coated samples, the OCP value of bare Mg alloy is the most stable, at about −1.52 V. In the beginning (first 24 h) of immersion test, the OCP values of Mg-P, Ca-P and CaMg-P were lower than that of the other samples. Sample ZnCaMg-P had the highest OCP in the beginning and then decreased to

−1.52 V at 36 h. Compared with Zn P and AZ31 Mg alloy, the OCP values of ZnMg-P, ZnCa-P and ZnCaMg-P are slightly higher, which may be caused by Zn existing in the conversion coatings. After about 3 d, the OCP values of all coated samples approached the OCP of Mg alloy substrate, indicating the coatings on Mg alloy could not provide complete coverage anymore.

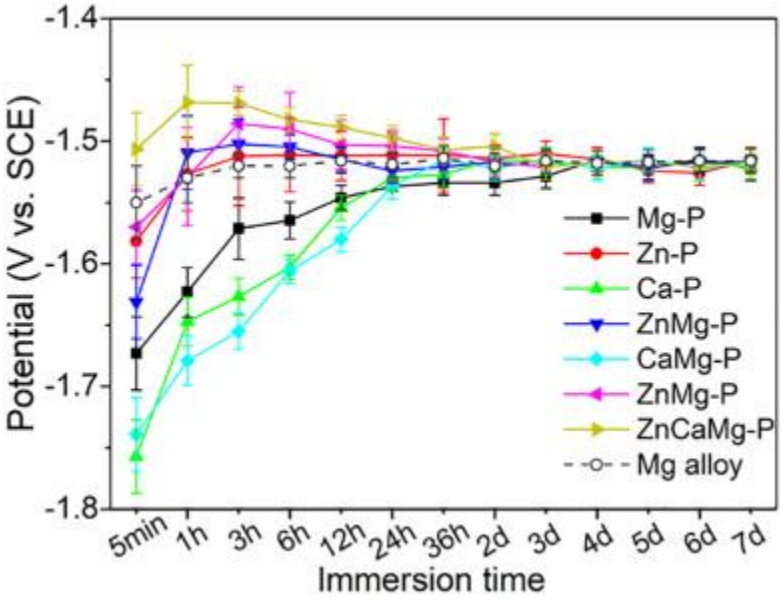

Fig. 9. OCP curves of all coated samples and AZ31 Mg alloy in Hanks' solution at 37 °C.

During the immersion test, EIS measurement was conducted to assess the corrosion performance of bare AZ31 Mg alloy and all coated samples. The results of long-term EIS test are presented in the forms of Nyquist plots (Fig. 10(a)-(h)) and Bode-phase plots (Fig. 10(a′)-(h′)). In order to fit

the EIS data, physical models and electrical equivalent circuits (EEC) are proposed and presented in Fig. 11. Because the time-constant dispersion [41] caused by surface heterogeneity [42,43], fractal geometry [44,45], electrode porosity [46,47], variation of coating and surface composition [48,49], two-dimensional (2D) and three-dimensional (3D) distribution [49], and geometry-induced current and potential distributions [[50], [51], [52]], the constant phase element (*CPE,* abbreviated as *Q* in this paper) was introduced [43,53] to fit the EIS data. Z_Q, the impedance of *Q* can be expressed as Eq. (2), in which *Y* is the constant admittance of *Q*, *j* is √−1, ω is the angular frequency and $\omega = 2\pi f$. When $n = 1$, *Q* represents pure capacitance; when $n = -1$, *Q* represents inductance (*L*). It was indicated that the low-frequency impedance limit (which is decided by the inductive response in the EIS test) is the crucial parameter of real corrosion rate [54,55], and the inductive loops at low-frequency are attributed to the relaxation of the adsorbed species Mg^{+}_{ads} [[56], [57], [58]] on the interface of electrolyte/electrode, which is often accompanied by rapid pitting corrosion [59]. Therefore, according to the Pébère model [57,58,60], element *L* was introduced to fit the inductive response in the EIS result.(2)ZQ=1Y·jω−n

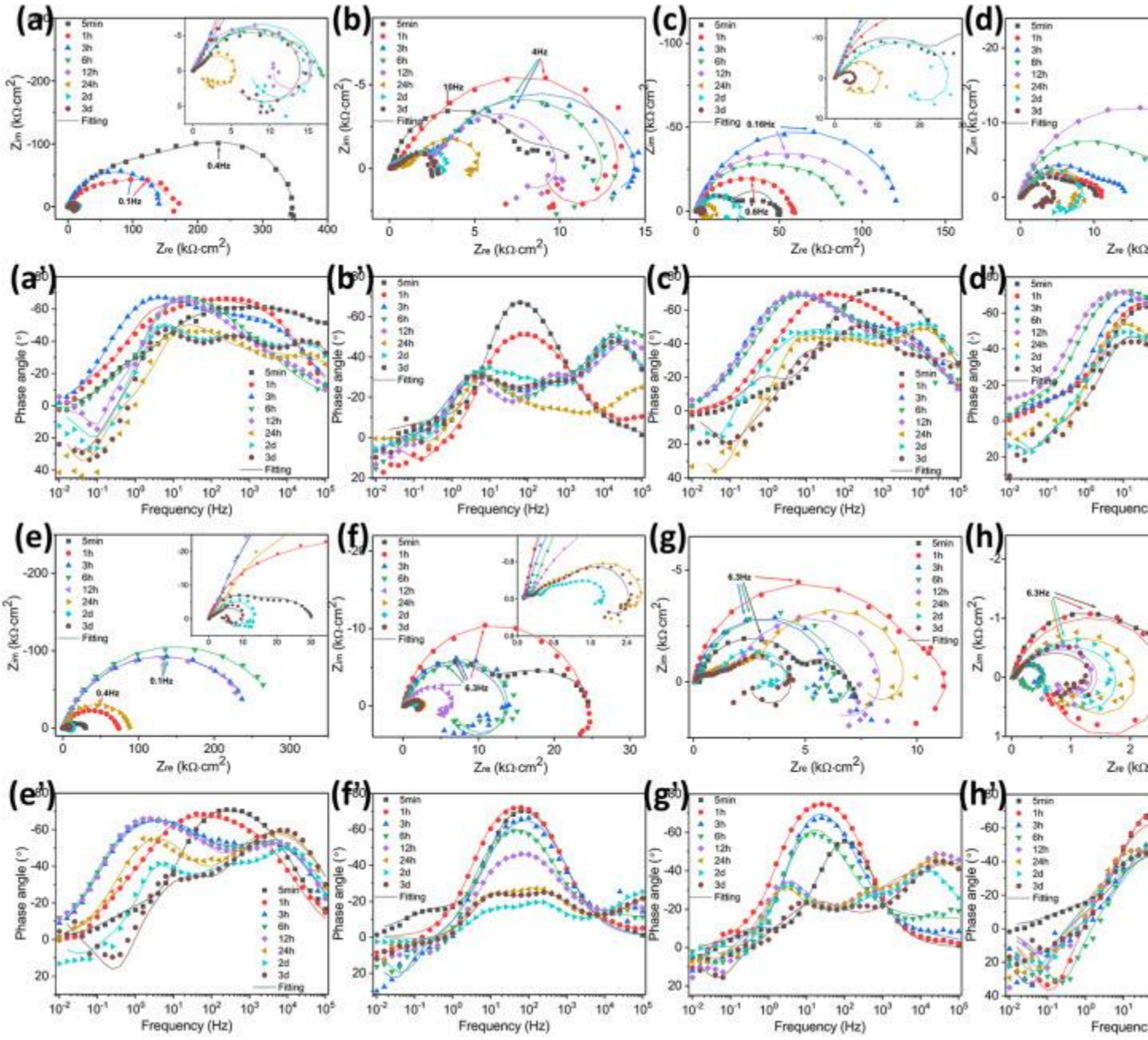

Fig. 10. EIS results of all coated samples and AZ31 Mg alloy. Nyquist plots and Bode phase-angle plots of (a)(a′) Mg-P, (b)(b′) Zn-P, (c)(c′) Ca-P, (d)(d′) ZnMg-P, (e)(e′) CaMg-P, (f)(f′) ZnCa-P, (g)(g′) ZnCaMg-P and (h)(h′) AZ31 Mg alloy.

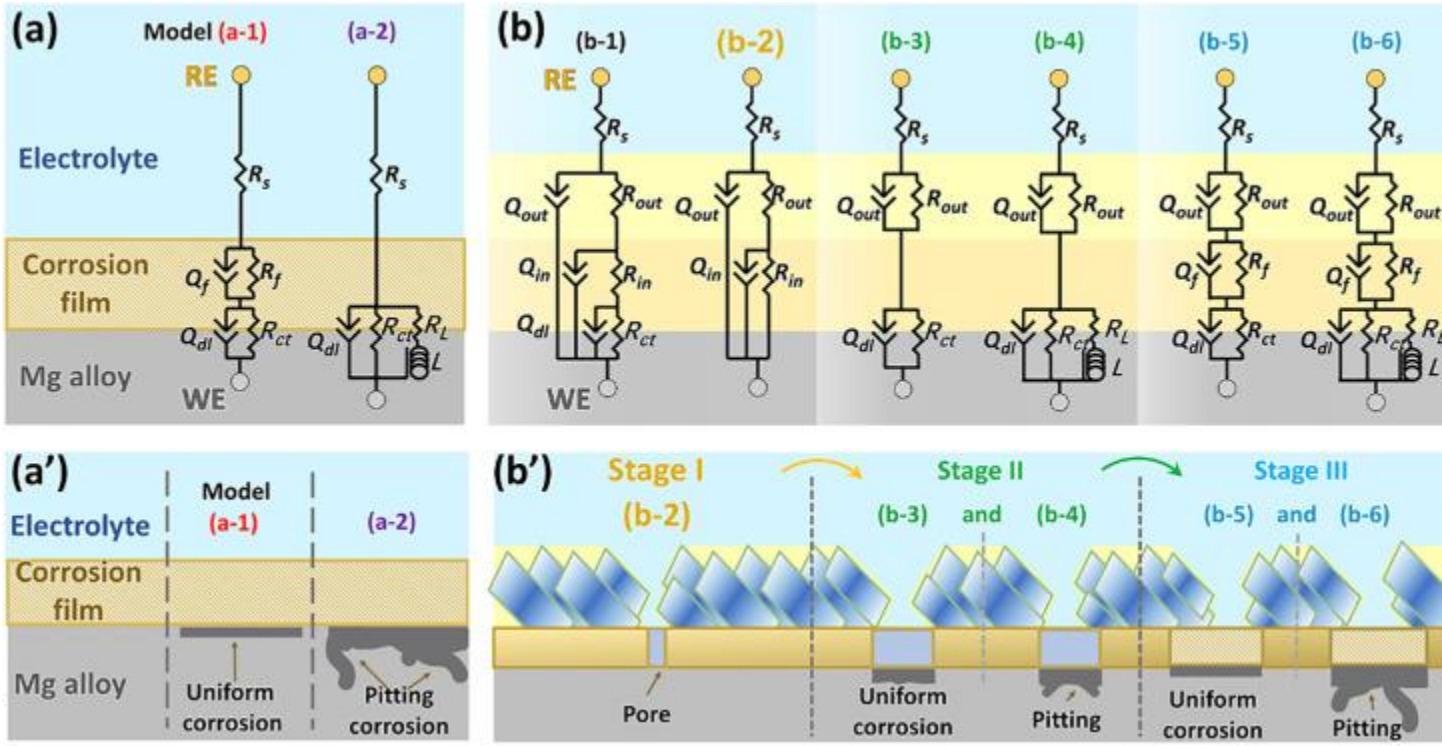

Fig. 11. (a) EEC models of AZ31 Mg alloy and (a') the corresponding physical models; (b) EEC models of coated samples and (b') the corresponding physical models.

As shown in the models (Fig. 11), Q_{dl}, Q_f, Q_{out} and Q_{in} correspond to the capacitive characters of the double layer at the substrate surface, corrosion film, outer layer and inner layer of the conversion coating, respectively. R_{ct}, R_f, R_{out} and R_{in} correspond to the resistances of charge-transfer, corrosion product film, the outer layer and inner layer of conversion coatings. The total impedance (Z_{tot}) of the EEC models in Fig. 11 is given in Eqs. (3), (11) (Z_Q is abbreviated as Q, Z_L is the impedance of L). The polarization resistances (R_p) in different EEC models are calculated using Eq. (11). The resistances in the EEC models obtained via fitting using the EIS data are presented in Fig. 11.

Model (a-1) in Fig. 11(a)(3)Ztot=RS+11Rf+1Qf+11Rct+1Qdl

Model (a-2) in Fig. 11(a)(4)Ztot=RS+11Rct+1Qdl+1RL+1ZL

Model (b-1) in Fig. 11(b)(5)Ztot=RS+11Qout+11Rout+11Qin+11Rin+11Qdl+1Rct

Model (b-2) in Fig. 11(b)(6)Ztot=RS+11Qout+1Rout+11Rin+1Qin

Model (b-3) in Fig. 11(b)(7)Ztot=RS+11Qout+1Rout+11Qdl+1Rct

Model (b-4) in Fig. 11(b)(8)Ztot=RS+11Qout+1Rout+11Qdl+1Rct+11RL+ZL

Model (b-5) in Fig. 11(b)(9)Ztot=RS+11Qf+1Rout+11Qf+1Rf+11Qdl+1Rct

Model (b-6) in Fig. 11(b)(10)Ztot=RS+11Qf+1Rout+11Qf+1Rf+11Qdl+1Rct+1RL+ZL

Polarization resistance(11)Rp=Ztot−Rsϖ=0

At the beginning of the corrosion process (5 min) of AZ31 Mg alloy, two obvious capacitive loops are appearing in the Nyquist plot (Fig. 10(h)) corresponding to the EEC model (a-1) in Fig. 11. With the increase of immersion time, the capacitive loop of the corrosion film at low-frequency decreases and is then replaced by an inductive loop gradually, and at the same time, the R_p of Mg alloy decreases from 3820 to 620 and 135 Ω·cm^2 at 1 h and 3 h, and then increases to 152 Ω·cm^2 at 6 h, to about 800 Ω·cm^2 at 12 h, and then maintains steady at this value to 3 d. As shown in Fig. 10 and Fig. 12, compared with the other samples, Mg-P has the largest R_p, up to 358 kΩ·cm^2 in the beginning (at 5 min). However, with the immersion test continued, the R_p of Mg-P decreases sharply to about 2 kΩ·cm^2 at 24 h and maintains at that value to 3 d. Compared with the other coatings, Ca-P and CaMg-P with a similar composition of DCPD have relatively stable and good corrosion resistance and the values of their R_p remain above 10 kΩ·cm^2 in the first 24 h during the test. Among the coatings Zn-P, ZnMg-P, ZnCa-P and ZnCaMg-P, ZnMg-P has relatively good corrosion resistance. Even its R_p is not as high as Mg

P, Ca P and CaMg-P, ZnMg-P keeps a very stable R_p during the whole EIS test.

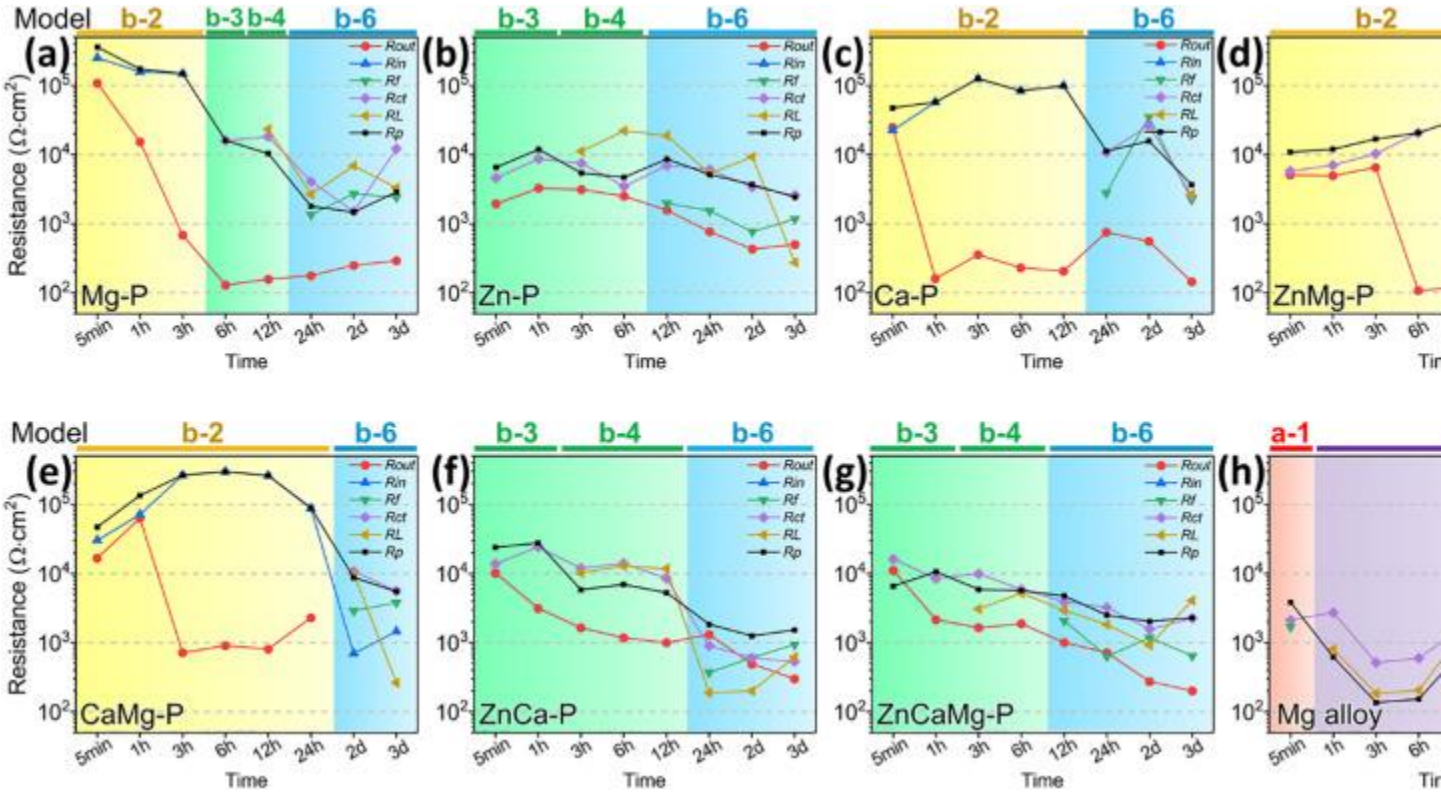

Fig. 12. Comparison of resistances (R_{out}, R_{in}, R_f, R_{ct} and R_p) from EIS fitting results of coated samples: (a) Mg-P, (b) Zn-P, (c) Ca-P, (d) ZnMg-P, (e) CaMg-P, (f) ZnCa-P, (g) ZnCaMg-P and (h) bare AZ31 Mg alloy.

After 3 d of immersion, all coatings have approximately the same values of R_p, about several $k\Omega \cdot cm^2$. Once the R_p of coated sample approaches the R_p of bare Mg alloy, Mg alloy substrate under conversion coating usually suffers from severely local corrosion which could not be accurately evaluated by EIS during the long-term corrosion. In order to evaluate the long-term corrosion behavior of different samples in greater detail after 3 d, hydrogen evolution measurement and surface morphologies study were performed.

Fig. 13(a) shows the hydrogen evolution volumes of bare AZ31 Mg alloy and coated samples in Hanks' solution at 37 °C. Fig. 13(b) shows the OM surface morphologies of coated samples and bare substrate AZ31 Mg alloy after 1 d, 3 d, 5 d, 10 d, 15 d of immersion. Compared with the coated samples, bare AZ31 Mg alloy suffers from severe filiform corrosion and pitting corrosion during the whole immersion test, and the OM images are consistent with the largest hydrogen evolution volume (12.8 mL at 15 d) as shown in Fig. 13(a). Besides bare Mg alloy, Mg-P, Ca-P, and CaMg-P also suffer from serious corrosion and the corresponding hydrogen evolution volumes are about 8.1, 7.1 and 5.7 mL respectively after 15 d immersion. On the other hand, the corrosion forms of Zn-P, ZnMg-P, ZnCa-P and ZnCaMg-P are dominated by pitting corrosion. Among all samples, ZnMg-P shows the best anti-corrosion performance as evidenced by the surface morphologies in Fig. 13(b) and the minimum hydrogen evolution volume (about 4.2 mL as shown in Fig. 13(a)) after 15 d immersion.

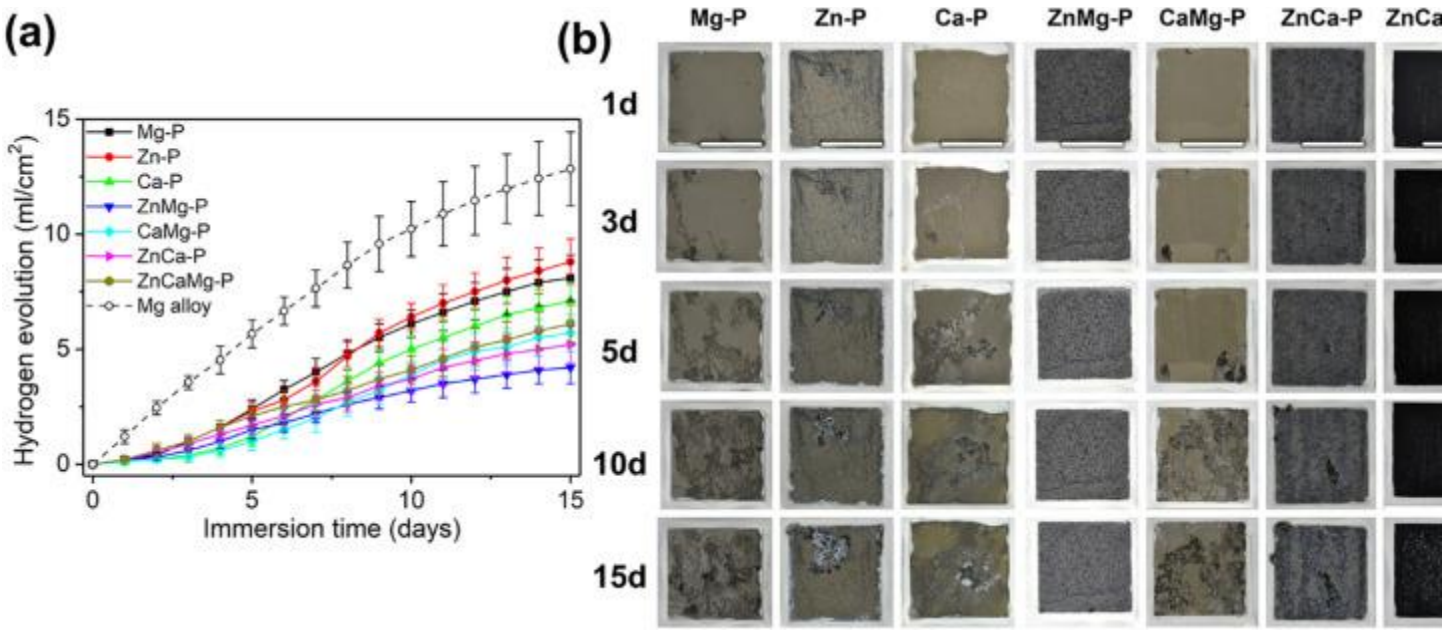

Fig. 13. **(a)** Hydrogen evolution volumes of coated samples and Mg alloy and **(b)** OM surface morphologies of coated samples and bare substrate AZ31 Mg alloy after 1, 3, 5, 10, 15 d of immersion test in Hanks' solution at 37 °C (the scales bar is 10 mm).

In order to investigate the micro corrosion morphologies of all samples and the corrosion products on their surfaces after the immersion test, SEM and EDS tests were conducted and the results are presented in Fig. 14 and Fig. 15. As shown in Fig. 14(h1)(h2), obvious filiform corrosion ribbons with an average width of about tens of micrometers appear on the surface of Mg alloy and pitting corrosion pores also form on the existing filiform corrosion ribbons after 3 days of immersion. With further corrosion, Mg alloy suffers from severe corrosion and a large amount of $Mg(OH)_2$ forms on the surface which results in dry riverbed-like massive cracks on its surface as shown in Fig. 14(h3) and (h4). The particle-like phosphates of Ca and Mg are always accompanied by severe corrosion as shown in Fig. 14(h5) and (h6), and the EDS results at point

H1 and H2 are presented in Fig. 15. Filiform corrosion appears on the surface of Mg P after 3 d; then phosphates of Ca and Mg precipitate on the dry riverbed corrosion surface after 7 d. The corroded surface after the whole immersion test is shown in Fig. 14(a1)-(a6). The EDS results at point A1 and A2 indicate phosphates of Ca and Mg formed on the corrosion product $Mg(OH)_2$. Among the CaP type of conversion coating, Ca-P and CaMg-P have a good ability to

induce the precipitations of phosphates of Ca and Mg after 15 d of immersion test which is similar to Mg-P as shown in Fig. 14(c5)(c6) and (e5)(e6). As for the ZnP type of conversion coatings, Zn-P, ZnMg-P, ZnCa-P and ZnCaMg-P are dominated by pitting corrosion rather than filiform corrosion during the immersion test and the amount of phosphate precipitated on their surfaces is obviously smaller than that on Mg-P, Ca-P and CaMg-P. Compared with the other samples, ZnMg-P has better corrosion resistance and the pits with 5 hundred microns diameter appear on its surface after 15 d of immersion as shown in Fig. 14(d5) and (d6). According to the EDS results of the particle-like phosphates of Ca and Mg in Fig. 15, the atomic ratio of Ca:Mg:P is about 2:1:2. Therefore its probable main phase is collinsite $Ca_2Mg(PO_4)_2 \cdot 2H_2O$, which may also contain some other forms of calcium magnesium phosphates, such as whitlockite $(Ca,Mg)_3(PO4)_2$ and carbonates.

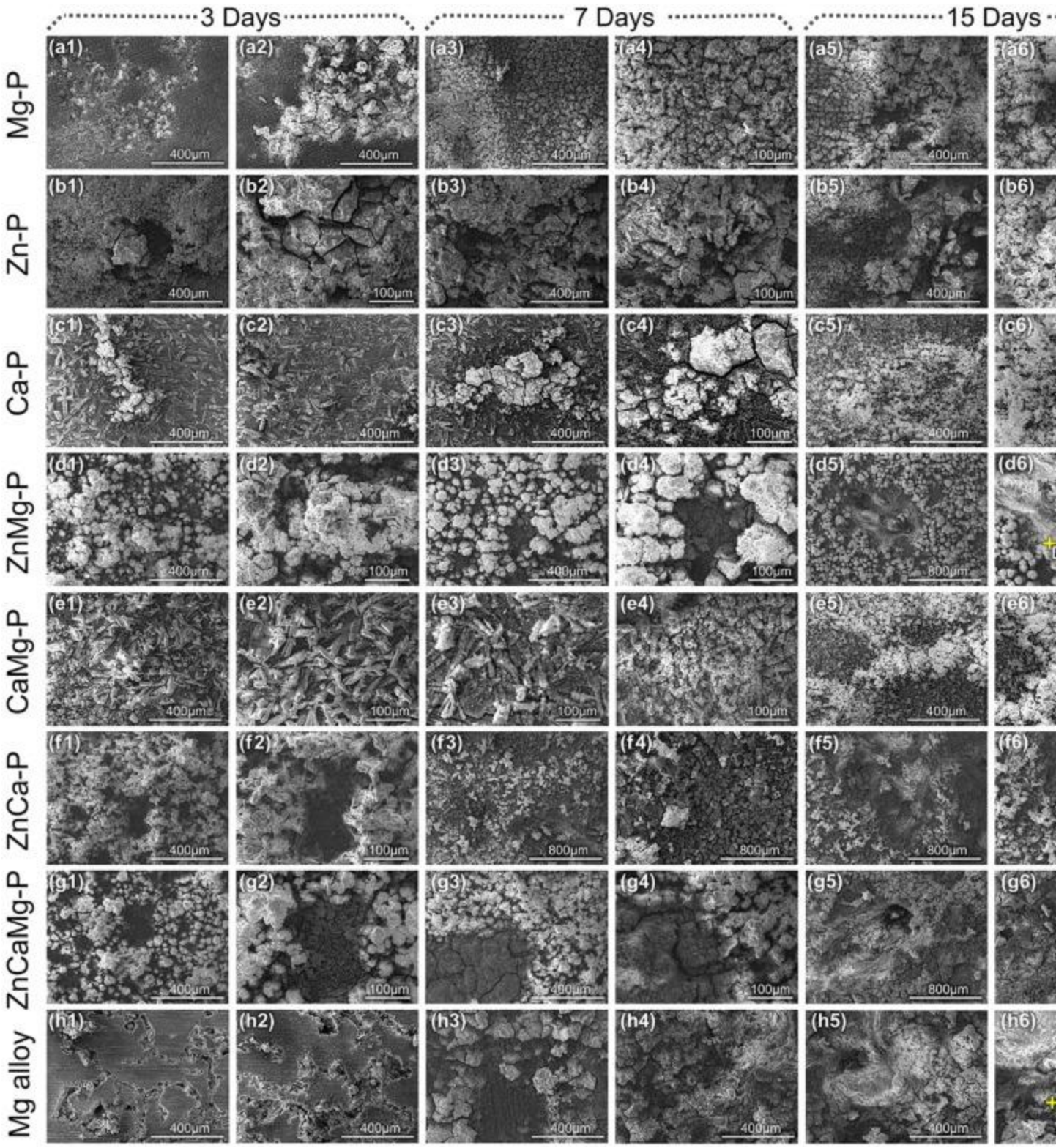

Fig. 14. Surface morphologies of all coated samples and Mg alloy immersed in Hanks' solution at 37 °C for 3, 7 and 15 days.

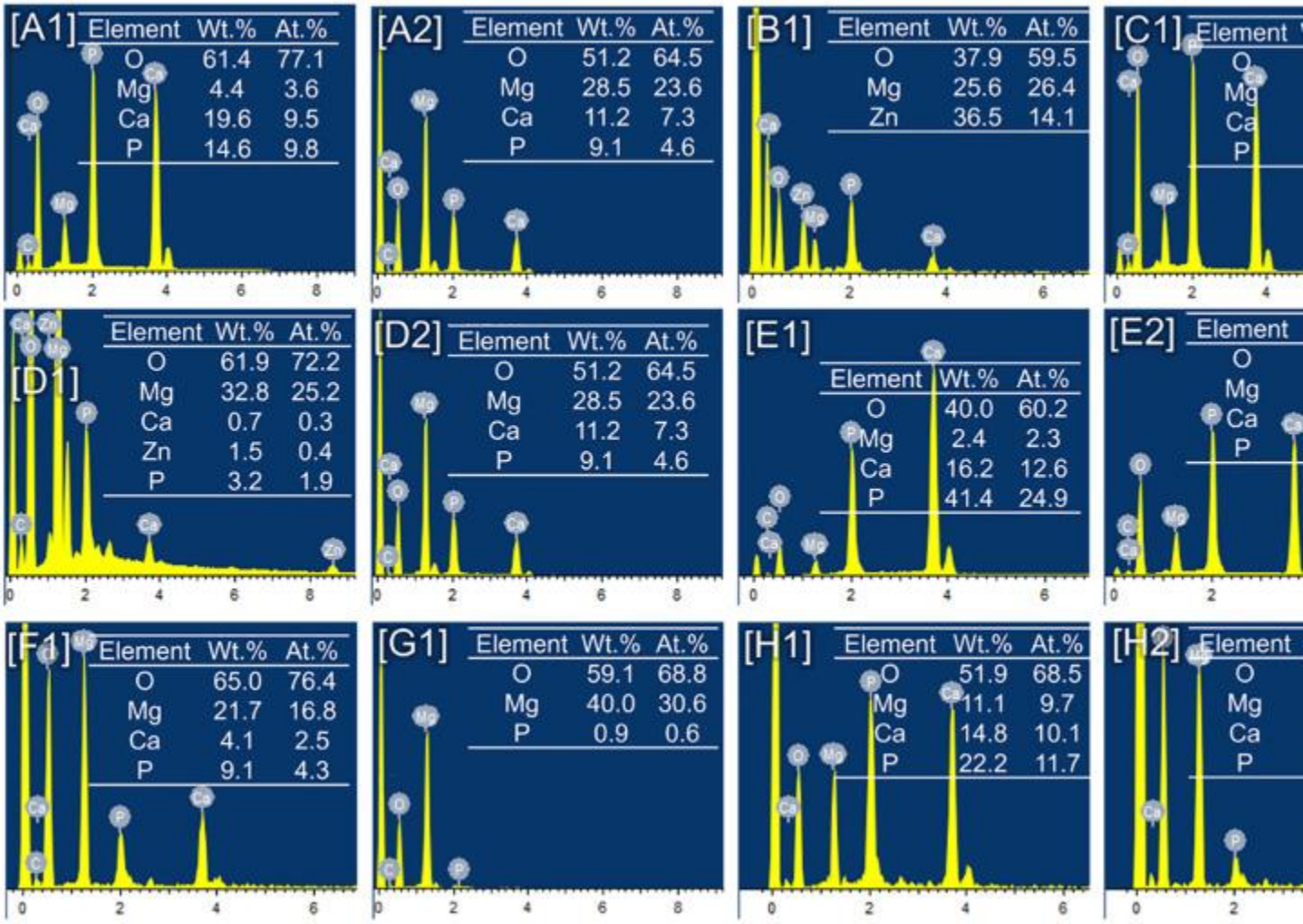

Fig. 15. EDS results corresponding to the tested points in Fig. 14.

4. Discussion

4.1. The formation mechanism and precipitation priority of conversion coatings

In order to investigate the formation mechanism of different conversion coatings, predominance area diagrams of magnesium phosphate, zinc phosphate and calcium phosphate are determined with a constant phosphate concentration of 0.2 mol/L at room temperature (25 °C) and the results are presented in Fig. 16.

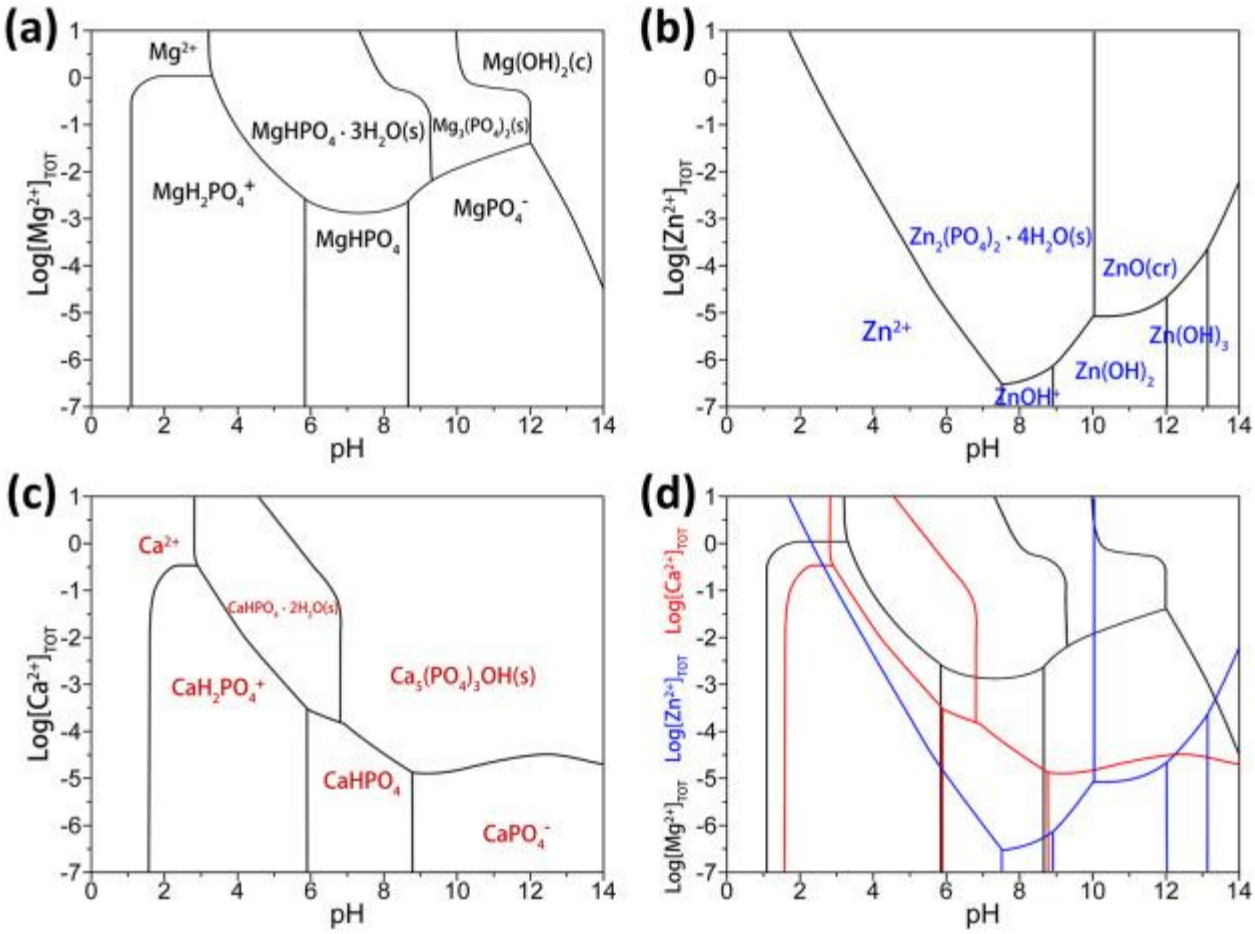

Fig. 16. Predominance area diagrams for solutions containing 0.2 mol/L phosphate at different concentrations of (a) Mg^{2+} ions (b) Zn^{2+} ions (c) Ca^{2+} ions and (d) combination of Mg^{2+}, Zn^{2+} and Ca^{2+} ions.

The formation process of phosphate conversion coatings on Mg alloy consists of two main steps: I. corrosion of Mg substrate and II. the precipitation of phosphates [22]. For Mg corrosion, in 1907 Turrentine [61] proposed an intermediate species of Mg with a valence lower than $n = 2$, and in 1954 Petty et al. [62] described it as "unipositive Mg". In 1866, Beetz [63] first found the anodic hydrogen evolution (AHE), and the Song, Atrens and Dietzel et al. [[64], [65], [66], [67]] explained the negative difference effect (NDE, which is also known as AHE) of Mg alloy during the corrosion, and the corrosion process of Mg alloy at free corrosion potential can be expressed as follows, which consists of electrochemical and chemical corrosion steps (Eqs. (12), (13), (14), (15), (16)) [57,64,68].

Anodic partial reaction I(12)Mg→Mg++e−

Anodic partial reaction II(13)kMg+→kMg2++ke−

Chemical reaction(14)1−kMg++1−kH+→1−kMg2++1−k/1H2

Cathodic reaction(15)1+kH++1+ke+→1+k/1H2

Total reaction(16)Mg+2H+→Mg2++H2g

Mg corrosion process consumes a large amount of H^+ ions and forms a high pH region near the substrate where phosphates are accelerated to precipitate on the Mg alloy substrate (Eqs. (17), (18), (19)) [22,69].(17)Mg2++H2PO4−+3H2O→MgHPO4·3H2Os+H+(18)3Zn2++2H2PO4−+4H2O→Zn3PO42·4H2Os+2H+(19)Ca2++H2PO4−+2H2O→CaHPO4·2H2Os+H+

According to the main phases of different conversion coatings, it is found that the addition of Zn^{2+} ions preferentially forms zinc phosphate and inhibits the formation of calcium phosphate and magnesium phosphate. On the other hand, the addition of Ca^{2+} ions inhibits the formation of magnesium phosphate. As shown in the predominance area diagram (Fig. 16(d)), the precipitation line of the boundary $Zn^{2+}/Zn_3(PO_4)_2$ in the zinc phosphate diagram is the lowest, then the boundary $Ca^{2+}/CaHPO_4$ in calcium phosphate diagram and the boundary $Mg^{2+}/MgHPO_4$ in the magnesium phosphate diagram is the highest. The precipitation sequence of different phosphates is $Zn_3(PO_4)_2 > CaHPO_4 > MgHPO_4$ which is consistent with their solubility product constants [70] (Table 4). In other words, the precipitation priority of conversion coatings is ZnP type > CaP type > MgP type.

Table 4. Solubility product constants (K_{sp}) of some compounds (25 °C).

Compounds	**$MgHPO_4$**	**$CaHPO_4$**	**$Zn_3(PO_4)_2$**	**$Mg(OH)_2$**
K_{sp}	1.5×10^{-6}	1.0×10^{-7}	9.0×10^{-33}	5.6×10^{-12}

From the OM images of conversion coatings in Fig. 4, the ZnCaMg-P coating is much darker than the other coatings, which may be caused by the formation of metallic Zn in the coatings [31]. The possible side reactions of Zn reduction, during the generation of ZnP type of coatings, are presented in Eqs. (20), (22). Eq. (20) indicates the possible electrochemical reaction of Zn formation, and Eqs. (21), (22) indicates the possible chemical reactions of Zn formation during the preparation of conversion coatings.(20)Zn2++2e−→Zn(21)Zn2++2Mg+→Zn+2Mg2+(22)Zn2++Mg→Zn+Mg2+

4.2. EIS response of pitting corrosion of Mg alloy

In the Nyquist plots, there are obvious decreases of initial angle (Φ) at high-frequency Nyquist plots of Mg alloy substrate after 1 day of immersion as shown in Fig. 10(h) and asymmetric peaks are observed in the Bode phase plots (Fig. 10(h′)). The phenomenon can be attributed to the macro-pores formed by filiform and pitting corrosion. In order to elucidate the phenomenon, a physical model and an EEC model are proposed and presented in Fig. 17(a). In the figure, R_s is electrolyte resistance, the mean length of pores is L, the thickness of an infinitesimal sliced layer is Δx, R_0 is pores resistance for one-unit length, Z_0 is surface impedance for one-unit area, KZ_0 is the impedance of outer surface for one-unit area and the N is the number of pores on one-unit area surface. The general form of the impedance of a pore (Z_{po}) can be expressed by Eq. (23) [47,71,72]. λ (Eq. (24)) is the penetrating depth of the electrical signal.(23)Zpo=R0Z0cothLλ(24)λ=Z0R0

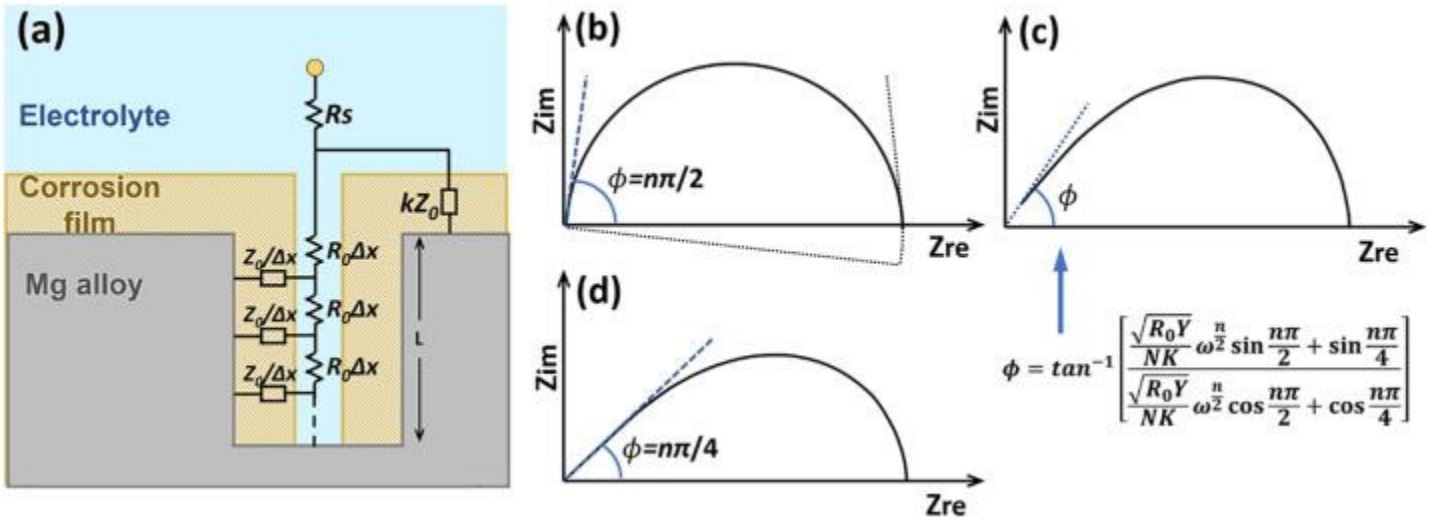

Fig. 17. (a) EEC model and physical model of Mg alloy in Hanks' solution after pit formation, (b) Nyquist plot of Mg electrode, (c) Nyquist plot of Mg electrode with pits, and (d) limiting Nyquist plot of Mg electrode with pits.

The total impedance (Z_{tot}) of the electrode with pores in the presence of electrolyte can be express by Eq. (25) according to the physical model and EEC model in Fig. 17(a).(25)Ztot=Rs+1KZ0+NZpo−1

When L is infinitesimal to λ, corresponding to the beginning of the immersion test, $\coth(L/\lambda)$ approaches λ/L and Z_{po} tends to Z_0/L. Therefore, Z_{tot} can be expressed by Eq. (26).

If NL approaches 0, Z_{tot} can be simplified to $Rs + KZ_0$, which corresponds to an electrode without pore.

When L is small compared with λ:(26)Ztot=Rs+K1+NKLZ0

when L is large compared with λ, $coth(L/\lambda)$ approaches 1 and Z_{tot} can be expressed by Eq. (27). Severe corrosion of Mg alloy results in an increase of n and K, and Z_{tot} will tend to Rs+R0Z0/N in the end.

When L is large compared with λ:(27)Ztot=Rs+KZ0R0Z0NKZ0+R0Z0

In order to investigate the expression of the initial angle (Φ) of Z_{tot} (Eq. (29)), Z_a is got from Z_{tot} by compensating solution resistance (R_s) as expressed in Eq. (28), and Z_a' and Z_a'' are the real and imaginary parts of Z_a respectively.(28)Za=Ztot−Rs(29)ϕ=tan−1Za″Za′

If the impedance response of Z_0 is dominated by a Q ($Z_Q = [Y(j\omega)^n]^{-1}$) at high-frequency, the phase angle formula of Z_a can be simplified to Eq.(30) below.(30)ϕ=tan−1R0YNKωn2sinnπ2+sinnπ4R0YNKωn2cosnπ2+cosnπ4when L is small compared with λ, Φ is nπ/2 where n equals to n_{dl} (the coefficient of Q_{dl}) as shown in Fig. 17(b). When L is large compared with λ, Φ can be calculated using Eq. (30).

When R0YNKωn2 is large compared with 1, Φ tends to nπ/2 as shown in Fig. 17(b).

When R0YNKωn2 approaches 1, Φ can be calculated using Eq. (30) as shown in Fig. 17(c).

When R0YNKωn2 is small with 1, Φ tends to nπ/4 as shown in Fig. 17(d).

After long-term immersion, severe pitting and filiform corrosion formed on Mg alloy caused the increase of pores (corresponding to increase of N) and decrease of the effect of the outer surface (corresponding to increasing of K) on the impedance response. Finally, the Nyquist plot of Z_{tot} tends to the form of R0Z0 as shown in Fig. 17(d).

4.3. Time-constant shielding (TCS) effect

Due to the specific relationship of time-constant of different circuits in the EEC, time-constant responses caused by different circuits may be depressed or merged in the EIS plots (time-constant τ corresponds the inverse of angular frequency (ω) of the extremum data point in the Nyquist plot, and the time-constant τ of three kinds of circuits are descripted by Eqs. (31), (33)). For example, in the first stage of EIS test of the MgP and CaP type coatings, as shown in Fig. 10 and Fig. 11, the capacitive loop of inner layer at low-frequency shield the capacitive loop of Mg alloy substrate. And the inductive loop of Mg alloy substrate shields the capacitive loop of corrosion film on the Mg alloy substrate. In this paper, this phenomenon is defined as time-

constant shielding (TCS) effect. In order to explain the impact of variation of time-constants on the EIS responses, three cases are introduced in Fig. 18(a), (b) and (c). In Fig. 18(a), the initial EEC model of $R_s(R_fQ_f)(R_{ct}Q_{dl}(LR_L))$ is used to simulate the Mg alloy substrate with corrosion product film. And in Fig. 18(b) and (c), two types of initial EEC models $R_s(Q_c(R_c(Q_{dl}R_{ct})))$ and $R_s(R_fQ_f)(R_{ct}Q_{dl})$ are chosen to represent the porous film and dense coating, because the electrolyte in the porous film and the dense coating are homogeneous penetration and local penetration respectively [41].

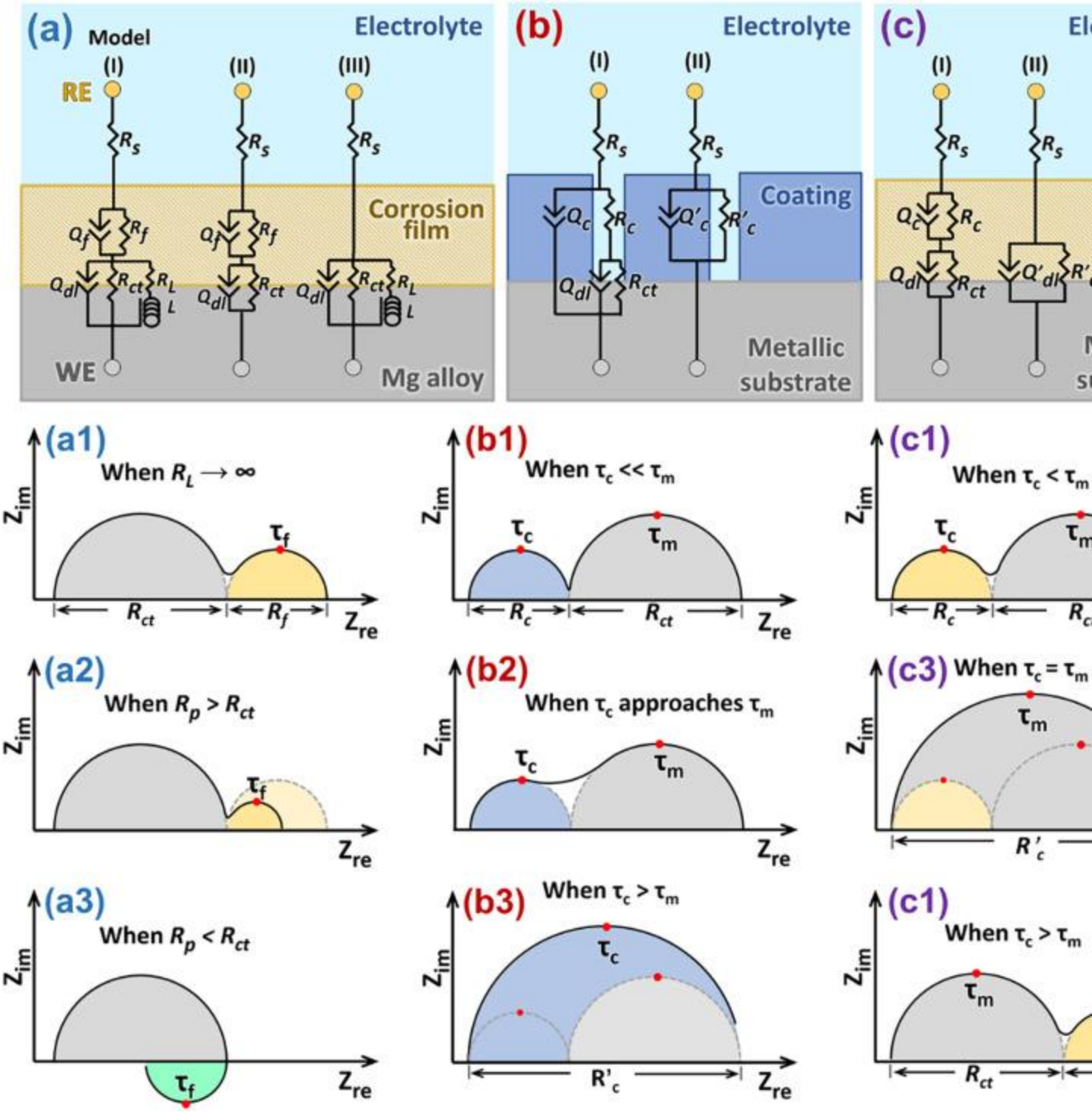

Fig. 18. (a) EEC models of corrosion film on Mg alloy substrate and the corresponding Nyquist plots if (a1) R_L approaches infinity, (a2) R_p is larger than R_{ct}, and (a3) R_p is less than R_{ct}. (b) EEC models (local penetration) of dense coating on the metallic substrate and the corresponding Nyquist plots if (b1) $\tau_c \ll \tau_m$, (b2) τ_c approaches τ_m, (b3) $\tau_c > \tau_m$. (c)

EEC models (uniform penetration) of porous coating on metallic substrate and the corresponding Nyquist plots if (c1) $\tau_c < \tau_m$, (c2) $\tau_c = \tau_m$, (c3) $\tau_c > \tau_m$.

For parallel circuit (*RC*)(31)τ=1ω=RC

For parallel circuit (*RQ*)(32)τ=1ω=RY01n

For series circuit *RL*(33)τ=1ω=LR

As shown in Fig. 18(a), for the porous corrosion product film on Mg alloy substrate, during the long-term immersion EIS test, the capacitive loop of corrosion film and the inductive loop of Mg alloy substrate are not observed on the Nyquist plots simultaneously (Fig. 10 (h)). If we assume the capacitive loop and the inductive loop have approximate time-constant (τ_f, indicated by the red point in Fig. 18(a1)(a2)(a3)) according to Eqs. (32), (33). EEC model (I) in Fig. 18(a) is proposed to simulate the general EIS responses, and its R_p is expressed in Eq. (34). As shown in Fig. 18(a1), if the Mg alloy substrate does not suffer from obvious severe corrosion and it is covered with the corrosion film uniformly, the resistance of R_L approaches infinite. Therefore R_p approaches $R_{ct} + R_f$ and the EEC model can be simplified to model (II) in Fig. 18(a). With the appearance of severe corrosion and an increase of heterogeneity of the corrosion film coverage, the decrease of R_L will change the capacitive loop into an inductive loop. As shown in Fig. 18(a2), if $R_p > R_{ct}$, the capacitive response is dominant at low-frequency and the corresponding EEC can be simplified to model (II) in Fig. 18(a). As shown in Fig. 18(a3), if $R_p < R_{ct}$, inductive response replaces capacitive response at low-frequency and the corresponding EEC can be simplified to model (III) in Fig. 18(a).

For model (I) in Fig. 18(a)(34)Rp=Rf+RctRLRct+RL

As shown in Fig. 18(b), for a dense coating with local penetration of electrolyte on a metallic substrate, the EEC model (I) in Fig. 18(b) is applied to simulate the EIS response (R_c and Q_c correspond to the resistance and capacity of that coating). The time-constants of parallel circuits of (R_cQ_c) and $(R_{ct}Q_{dl})$ are denoted as τ_c and τ_m respectively as indicated in Fig. 18(b1)(b2)(b3) by the red points. If τ_m is much bigger than τ_c, as shown in Fig. 18(b1), two obvious capacitive loops can be observed on the Nyquist plot. If τ_c increases and approaches τ_m (Fig. 18(b2)), the boundary between the two capacitive loops will disappear gradually. Once the τ_c is larger than τ_m (Fig. 18(b3)), the capacitive loop of $(R_{ct}Q_{dl})$ will merge with the capacitive loop of (R_cQ_c). Then the EIS results can be fitted by the EEC model (II) in Fig. 18(b), and the resistance of the new capacitive loop (R_c') equals $R_c + R_{ct}$. Mansfeld [73]

gave a similar simulation result of this phenomenon. This phenomenon is often observed in EIS tests of organic coatings [73,75] and other kinds of dense coatings such as sol-gel coating [76] on metallic substrates.

As shown in Fig. 18(c), for a porous coating with uniform penetration of electrolyte on a metallic substrate, the EEC model (I) in Fig. 18(c) (differing from the model (I) in Fig. 18(b)) is chosen to simulate the EIS response. The time-constants of parallel circuits of (R_cQ_c) and ($R_{ct}Q_{dl}$) in Fig. 18(c) are denoted as τ_c and τ_m. If $\tau_c < \tau_m$, capacitive loops of (R_cQ_c) and ($R_{ct}Q_{dl}$) form on the Nyquist plot at high-frequency and low-frequency respectively, as shown in Fig. 18(c1).

If $\tau_c = \tau_m$, capacitive loops of (R_cQ_c) and ($R_{ct}Q_{dl}$) merge together and form one loop in the Nyquist plot in Fig. 18(c2), corresponding to model (II) in Fig. 18(c). If $\tau_c > \tau_m$, as shown in Fig. 18(c3) capacitive loops of ($R_{ct}Q_{dl}$) and (R_cQ_c) form in the Nyquist plot at high-frequency and low-frequency in contrast to the results in Fig. 18(c1).

Therefore the conclusion can be drawn as below:

1. Once parallel circuit (R_fQ_f) and series circuit LR_L in the EEC model have approximate time-constants, as shown in Fig. 18(a), the EIS responses (capacitive or inductive loops in Nyquist plot) of the circuit *(R_fQ_f)* and circuit LR_L can replace each other with the variation of R in their circuits. That is why the EIS responses of circuits of LR_L and (R_fQ_f) were not observed in the Nyquist plots of bare Mg alloy simultaneously in this work.
2. For locally penetrated dense coating on a metallic substrate, as shown in Fig. 18(b), once the time-constant of coating is larger than that of the metallic substrate, there will be only one capacitive response appearing on the EIS result. The resistance of the new capacitive loop equals the sum of coating resistance and charge-transfer resistance of the substrate. That is why the EIS response of ($R_{ct}Q_{dl}$) was shielded by the dense inner layer of the conversion coatings (such as Mg-P, Ca-P and CaMg-P) at the beginning of EIS test shown in Fig. 10.
3.

For uniformly penetrated porous coating on the metallic substrate, as shown in Fig. 18(c), except that the substrate has the same time-constant of coating, the capacitive loops of the substrate and the coating appear on the Nyquist plot from high-frequency to low-frequency by their time-constant.

4.4. Corrosion mechanism of conversion coatings and Mg alloy substrate

According to the corrosion mechanism and the EIS results, as shown in Fig. 11(b'), the corrosion processes of conversion coatings can be separated into three main stages: (I) protection period, (II) breakdown period, (III) corrosion product formation period. In the protection period, conversion coating provides effective protection and only a little electrolyte penetrates outer layer and inner layer of the conversion coating. Due to the locally penetrated inner layer, according to the time-constant shielding effect (TCS), a large time-constant of the inner layer may cover the response of the Mg alloy substrate. Therefore model (b-2) replaces (b-1) in Fig. 11 to fit the EIS results. With the enlargement of pores in the inner layer, the protection of the inner layer is reduced and its time-constant also decreases. Once the inner layer breaks down severely, the conversion coating moves into stage II, the breakdown period. As the inner layer and outer layer have similar composition, the EIS response of the inner layer disappears and the response of the substrate appears at the same time corresponding to the EEC model (b-3) in Fig. 11. Finally, with the further corrosion of Mg alloy, the corrosion product precipitates on the substrate and its EIS response appears at medium-low-frequency as shown in the Bode phase plots in Fig. 10.

If we assume that the corrosion of Mg alloy is dominated by pitting corrosion and filiform corrosion simultaneously during long-term corrosion, as shown in Fig. 19(a), the filiform corrosion (black arrows) propagates in two dimensions of X and Y, and pitting corrosion (blue arrow) propagates in one dimension of Z. Therefore the corrosion rate of Mg alloy (C_r) can be express qualitatively by the corrosion rate formula Eq. (35) in which k is a constant, C_{fili} and C_{pit} are the propagation rates of the top ends of filiform corrosion and pitting corrosion.(35)Cr=k·Cfili2·Cpit

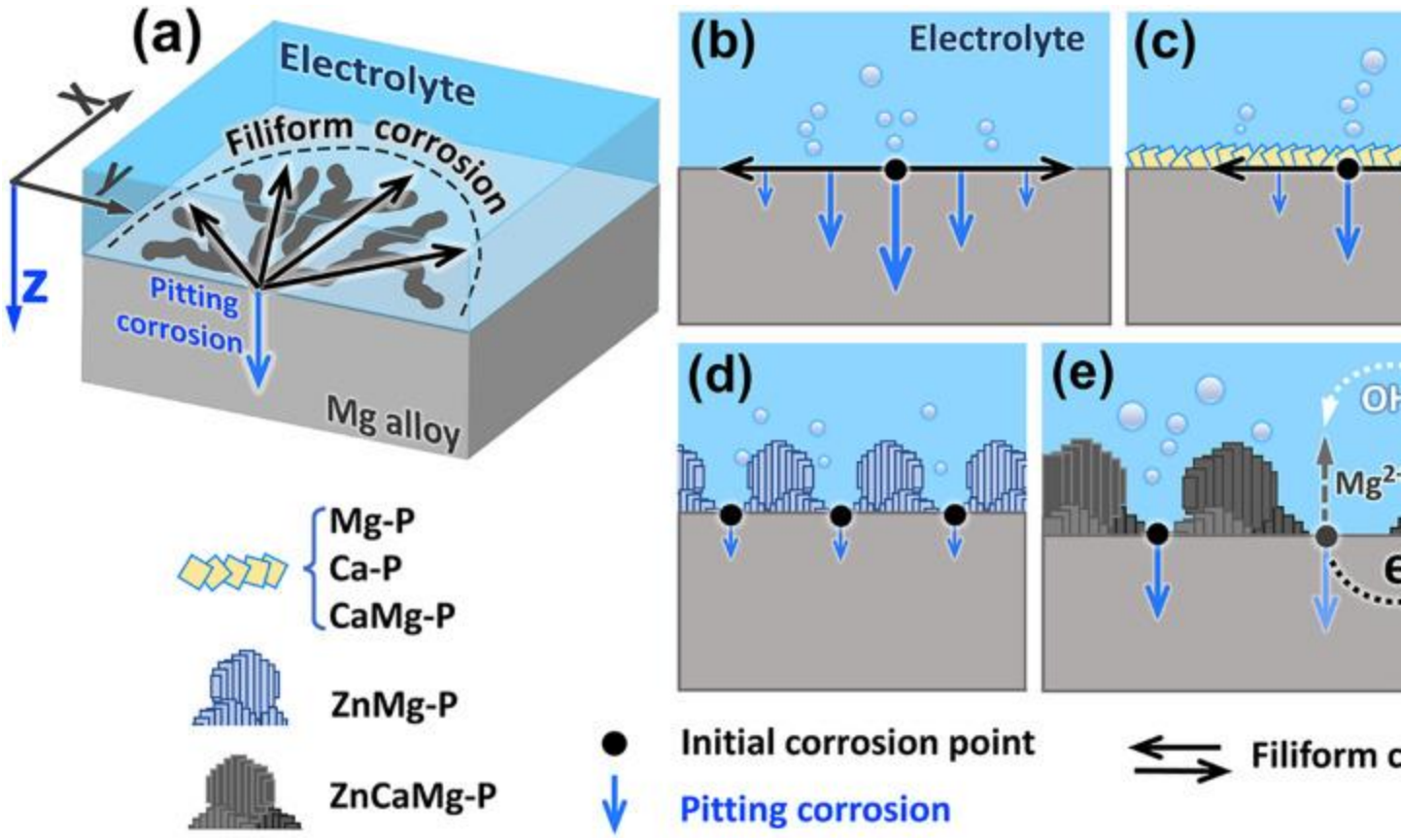

Fig. 19. Schematic illustration of long-term corrosion: (a) filiform corrosion and pitting corrosion, and corrosion mechanism of (b) Mg alloy; (c) Mg-P, Ca-P and CaMg-P conversion coating; (d) ZnMg-P and (e) ZnCaMg-P conversion coating during long-term immersion test.

For bare Mg alloy, as shown in Fig. 19(b), filiform corrosion and pitting corrosion develop from the initial corrosion point simultaneously. For the Mg-P, Ca-P and CaMg-P coatings (which are composed of $MgHPO_4 \cdot 3H_2O$ or DCPD), as shown in Fig. 19(c), even they can provide effective protection at the beginning, once breakdown Mg alloy substrate still suffers from filiform corrosion and pitting corrosion, which can be explained by that the coating is thinner and easier to dissolve. For ZnMg-P and ZnCaMg-P coatings which are composed of particle-like $Zn_3(PO4)_2 \cdot 4H_2O$, as shown in Fig. 2(d) and (e), because $Zn_3(PO4)_2 \cdot 4H_2O$ has extremely low solubility and high structural stability, filiform corrosion is hard to expand from the initial corrosion points on the substrate and therefore only pitting corrosion dominates in the overall corrosion rate. According to the Eq. (35), the decrease of C_{fili} can reduce the overall corrosion rate directly. Although ZnMg-P and ZnCaMg-P coatings have a similar composition and

structure, ZnCaMg-P suffers from obvious pitting corrosion as shown in Fig. 13(b) and 14. This phenomenon can be explained by the illustration in Fig. 19(e). Due to the small amount of metallic Zn in the coating, ZnCaMg-P and the exposure of Mg alloy substrate consists of microcell galvanic corrosion couple. As shown in Fig. 19(e), the anodic oxidation reaction (Eq. (37)) occurs on the initial corrosion point of Mg alloy substrate forming Mg ions and providing electrons to the cathode. Meanwhile, a cathodic reduction reaction (Eq. (36)) takes place on the ZnCaMg-P coating and hydrogen forms on its surface. The whole reaction can be expressed as Eq. (38). Therefore with a similar structure, ZnCaMg-P suffers from severer corrosion than ZnMg-P.

Cathodic reaction(36)$2H_2O+2e^- \rightarrow H_2+2OH^-$

Anodic reaction(37)$Mg \rightarrow Mg^{2+}+2e^-$

Overall reaction(38)$Mg+2H_2O \rightarrow Mg^{2+}+H_2+2OH^-$

4.5. Biocompatibility of conversion coatings

Based on the analysis of the cell viability test result in Fig. 7, CaP type coatings (Ca P and CaMg-P) show excellent biocompatibility which may be attributed to their composition of DCPD. DCPD as an important biomaterial in the field of bone cement [77] because it has excellent biodegradability and biocompatibility [78] and its degradation products can provide crucial Ca and P source for regeneration of bone tissues. There is limited research on the comparison of the effects of the coating types of MgP, CaP and ZnP on the precipitation of calcium and magnesium phosphates (its general composition probably is $Ca_2Mg(PO_4)_2 \cdot 2H_2O$). From the surface morphologies of all conversion coatings after long-term immersion of 15 d (Fig. 14), the amounts of precipitations on conversion coatings of MgP type (Mg-P) and CaP type (Ca-P and CaMg-P) are larger than that on ZnP type (Zn-P, ZnMg-P, ZnCa-P and ZnCaMg-P) conversion coatings. There are two probable reasons to explain the disparity of phosphates of calcium and magnesium precipitation on different type coatings:

1.

Compared with ZnP type coatings, the MgP type and CaP type coatings have larger solubility and are easier to dissolve. Therefore the destruction of conversion coatings promotes the alkalization near Mg alloy substrate and accelerates the precipitation of phosphates of calcium and magnesium from the Hanks' solution.

2.

MgP type and CaP type coatings have a similar composition with the precipitation of phosphates from Hanks' solution, which decreases the driving force of nucleation and growth of precipitation and therefore accelerates the precipitation during the immersion test.

4.6. Summary of conversion coatings.

As a summary, the comparative performance of various types of conversion coatings is shown in Table 5 below:

Table 5. Property summaries of coated samples and bare Mg alloy (A means the performance is higher than other, C means the performance is obviously lower than other, B means the performance is in-between, in other words, A > B > C).

	Sample	**Mg-P**	**Zn-P**	**Ca-P**	**MgZn-P**	**MgCa-P**	**ZnCa-P**	**MgZnCa-P**	**Mg alloy**
Properties	Coating Type	MgP	ZnP	CaP	ZnP	CaP	ZnP	ZnP	–
	Thickness (μm)	~17	~55	~15	~55	~50	~125	~73	–
	Adhesion (Mpa)	9.4 ± 1.1	1.8 ± 0.6	7.8 ± 1.5	5.6 ± 1.2	5.2 ± 1.3	2.5 ± 1.3	6.3 ± 0.7	–
	Biocompatibility	B	B	A	B	A	B	B	C
	Short-term (before 3d) Corrosion resistance	A	B	A	B	A	B	B	C

Sample	Mg-P	Zn-P	Ca-P	MgZn-P	MgCa-P	ZnCa-P	MgZnCa-P	Mg alloy
Long-term (on 15d) Corrosion resistance	B	B	B	A	B	B	B	C

5. Conclusions

(1)

The main phase of MgP type coating (including Mg P) is newberyite ($MgHPO_4 \cdot 3H_2O$), the main phase of CaP type coatings (including Ca-P and CaMg-P) is dicalcium phosphate dehydrate (DCPD, $CaHPO_4 \cdot 2H_2O$), and the main phase of ZnP type coatings (including Zn-P, ZnMg-P, ZnCa-P and ZnCaMg-P) is zinc phosphate hydrate ($Zn_3(PO_4)_2 \cdot 4H_2O$).

(2)

The precipitation of ZnP type coating on the Mg alloy substrate inhibits the generation of MgP type and CaP type conversion coatings, and the precipitation of CaP type coating inhibits the generation of MgP type coatings. In other words, the order of conversion coating generation priority is ZnP type > CaP type > MgP type.

(3)

By analyzing the morphologies of different coatings and their corrosion resistance, we can get several general rankings of the three types of conversion coatings: for thickness: ZnP type > CaP type > MgP type, for compactness: MgP type > CaP type > ZnP type, and for long-term corrosion resistance: ZnP type > CaP type > MgP type.

(4)

Mg alloy substrate, MgP type and CaP type conversion coatings suffer from mixed corrosion forms of filiform and pitting corrosion during the long-term immersion in

Hanks' solution, while the main corrosion form of ZnP type coatings (Zn P, ZnMg-P, ZnCa-P and ZnCaMg-P) is pitting corrosion. ZnMg-P has the optimal anticorrosion performance because its most stable structure effectively inhibits the propagation of filiform corrosion.

(5)

According to the cell viability test result, compared with ZnP, MgP type coatings and bare Mg alloy substrate, CaP type coatings have better biocompatibility.

CRediT authorship contribution statement

Wei Zai: Methodology, Investigation, Data curation, Writing - original draft.**Xiaoru Zhang:**Writing - review & editing.**Yingchao Su:**Writing - review & editing.**H.C. Man:**Resources, Writing - review & editing.**Guangyu Li:**Resources, Writing - review & editing.**Jianshe Lian:**Resources, Writing - review & editing.

Declaration of competing interest

The authors declare that they have no known competing for financial interests or personal relationships that could have appeared to influence the work reported in this paper.

Acknowledgments

The work described in this paper was supported by the National Natural Science Foundation of China (Grant Nos. 31070841, 51705195).

References

[1] L. Rodrigues **Inhibition of bacterial adhesion on medical devices**

Bact. Adhes. (2011), pp. 351-367, 10.1007/978-94-007-0940-9

[2] D. Bellucci, V. Cannillo, A. Cattini, A. Sola

A new generation of scaffolds for bone tissue engineering

Ind. Ceram. (2011), p. 31

[3] A.R. Boccaccini, J.J. Blaker

Bioactive composite materials for tissue engineering scaffolds

Expert Rev. Med. Devices., 2 (2005), pp. 303-317, 10.1586/17434440.2.3.303

[4] V. Mouriño, A.R. Boccaccini

Bone tissue engineering therapeutics: controlled drug delivery in three-dimensional scaffolds

J. R. Soc. Interface, 7 (2010), pp. 209-227, 10.1098/rsif.2009.0379

[5] F. Witte

Reprint of: the history of biodegradable magnesium implants: a review

Acta Biomater., 23 (2015), pp. S28-S40, 10.1016/j.actbio.2015.07.017

[6] . Witte, J. Fischer, J. Nellesen, H.A. Crostack, V. Kaese, A. Pisch, F. Beckmann, H. Windhagen

In vitro and in vivo corrosion measurements of magnesium alloys

Biomaterials, 27 (2006), pp. 1013-1018, 10.1016/j.biomaterials.2005.07.037

[7] M.P. Staiger, A.M. Pietak, J. Huadmai, G. Dias

Magnesium and its alloys as orthopedic biomaterials: a review

Biomaterials, 27 (2006), pp. 1728-1734, 10.1016/j.biomaterials.2005.10.003

[8] R. Zeng, W. Dietzel, F. Witte, N. Hort, C. Blawert

Progress and challenge for magnesium alloys as biomaterials

Adv. Eng. Mater., 10 (2008), pp. 3-14, 10.1002/adem.200800035

[9] C. Castellani, R.A. Lindtner, P. Hausbrandt, E. Tschegg, S.E. Stanzl-Tschegg, G. Zanoni, S. Beck, A.M. Weinberg

Bone-implant interface strength and osseointegration: biodegradable magnesium alloy versus standard titanium control

Acta Biomater., 7 (2011), pp. 432-440, 10.1016/j.actbio.2010.08.020

[10] G. Song

Control of biodegradation of biocompatable magnesium alloys

Corros. Sci., 49 (2007), pp. 1696-1701, 10.1016/j.corsci.2007.01.001

[11] S. Shadanbaz, G.J. Dias

Calcium phosphate coatings on magnesium alloys for biomedical applications: a review

Acta Biomater., 8 (2012), pp. 20-30, 10.1016/j.actbio.2011.10.016

[12] N.T. Kirkland, J. Lespagnol, N. Birbilis, M.P. Staiger

A survey of bio-corrosion rates of magnesium alloys

Corros. Sci., 52 (2010), pp. 287-291, 10.1016/j.corsci.2009.09.033

[13] X.B. Chen, N. Birbilis, T.B. Abbott

A simple route towards a hydroxyapatite–Mg(OH)2 conversion coating for magnesium

Corros. Sci., 53 (2011), pp. 2263-2268, 10.1016/j.corsci.2011.03.008

[14] E. Zhang, D. Yin, L. Xu, L. Yang, K. Yang

Microstructure, mechanical and corrosion properties and biocompatibility of Mg-Zn-Mn alloys for biomedical application

Mater. Sci. Eng. C., 29 (2009), pp. 987-993, 10.1016/j.msec.2008.08.024

[15] L.Y. Li, L.Y. Cui, R.C. Zeng, S.Q. Li, X.B. Chen, Y. Zheng, M.B. Kannan

Advances in functionalized polymer coatings on biodegradable magnesium alloys — a review

Acta Biomater., 79 (2018), pp. 23-36, 10.1016/j.actbio.2018.08.03016]

[16] X.J. Cui, X.Z. Lin, C.H. Liu, R.S. Yang, X.W. Zheng, M. Gong

Fabrication and corrosion resistance of a hydrophobic micro-arc oxidation coating on AZ31 Mg alloy

Corros. Sci., 90 (2015), pp. 402-412, 10.1016/j.corsci.2014.10.041

[17] H. Duan, K. Du, C. Yan, F. Wang

Electrochemical corrosion behavior of composite coatings of sealed MAO film on magnesium alloy AZ91D

Electrochim. Acta, 51 (2006), pp. 2898-2908, 10.1016/j.electacta.2005.08.026

[18] A.L.K. Tan, A.M. Soutar, I.F. Annergren, Y.N. Liu

Multilayer sol-gel coatings for corrosion protection of magnesium

Surf. Coatings Technol., 198 (2005), pp. 478-482, 10.1016/j.surfcoat.2004.10.066

[19] F. Hollstein, R. Wiedemann, J. Scholz

Characteristics of PVD-coatings on AZ31hp magnesium alloys

Surf. Coatings Technol., 162 (2003), pp. 261-268, 10.1016/S0257-8972(02)00671-0

[20] G. Wu, X. Zeng, G. Yuan

Growth and corrosion of aluminum PVD-coating on AZ31 magnesium alloy

Mater. Lett., 62 (2008), pp. 4325-4327, 10.1016/j.matlet.2008.07.014

[21] C. Christoglou, N. Voudouris, G.N. Angelopoulos, M. Pant, W. Dahl

Deposition of aluminium on magnesium by a CVD process

Surf. Coatings Technol., 184 (2004), pp. 149-155, 10.1016/j.surfcoat.2003.10.065

[22] W. Zai, Y. Su, H.C. Man, J. Lian, G. Li

Effect of pH value and preparation temperature on the formation of magnesium phosphate conversion coatings on AZ31 magnesium alloy

Appl. Surf. Sci. (2019), 10.1016/j.apsusc.2019.05.309

[23] Y. Su, G. Li, J. Lian

A chemical conversion hydroxyapatite coating on AZ60 magnesium alloy and its electrochemical corrosion behaviour

Int. J. Electrochem. Sci., 7 (2012), pp. 11497-11511

[24] Y. Su, Y. Su, W. Zai, G. Li, C. Wen

In vitro degradation behaviors of manganese-calcium phosphate coatings on an Mg-Ca-Zn alloy

Scanning (2018), 10.1155/2018/6268579

[25] T. Ishizaki, I. Shigematsu, N. Saito

Surface & coatings technology anticorrosive magnesium phosphate coating on AZ31 magnesium alloy

Surf. Coat. Technol., 203 (2009), pp. 2288-2291, 10.1016/j.surfcoat.2009.02.026

[26] N. Van Phuong, M. Gupta, S. Moon

Enhanced corrosion performance of magnesium phosphate conversion coating on AZ31 magnesium alloy

Trans. Nonferrous Metals Soc. China, 27 (2017), pp. 1087-1095, 10.1016/S1003-6326(17)60127-4

[27] Y. Su, Y. Guo, Z. Huang, Z. Zhang, G. Li, J. Lian, L. Ren

Preparation and corrosion behaviors of calcium phosphate conversion coating on magnesium alloy

Surf. Coatings Technol., 307 (2016), pp. 99-108, 10.1016/j.surfcoat.2016.08.065

[28] Y. Su, Y. Su, Y. Lu, J. Lian, G. Li

Composite microstructure and formation mechanism of calcium phosphate conversion coating on magnesium alloy

J. Electrochem. Soc., 163 (2016), pp. G138-G143, 10.1149/2.0801609jes

[29] L. Xu, F. Pan, G. Yu, L. Yang, E. Zhang, K. Yang

In vitro and in vivo evaluation of the surface bioactivity of a calcium phosphate coated magnesium alloy

Biomaterials, 30 (2009), pp. 1512-1523, 10.1016/j.biomaterials.2008.12.001

[30] R. Zeng, Z. Lan, L. Kong, Y. Huang, H. Cui

Characterization of calcium-modified zinc phosphate conversion coatings and their influences on corrosion resistance of AZ31 alloy

Surf. Coatings Technol., 205 (2011), pp. 3347-3355, 10.1016/j.surfcoat.2010.11.027

[31] L.Y. Niu, Z.H. Jiang, G.Y. Li, C.D. Gu, J.S. Lian

A study and application of zinc phosphate coating on AZ91D magnesium alloy

Surf. Coatings Technol., 200 (2006), pp. 3021-3026, 10.1016/j.surfcoat.2004.10.119

[32] Duan, L. Yang, S. Liao, C. Zhang, X. Lu, Y. Yang, B. Zhang, Y. Wei, T. Zhang, B. Yu, X. Zhang, F. Wang

Designing for the chemical conversion coating with high corrosion resistance and low electrical contact resistance on AZ91D magnesium alloy

Corros. Sci., 135 (2018), pp. 197-206, 10.1016/j.corsci.2018.02.051

[33] X.B. Chen, N. Birbilis, T.B. Abbott

Effect of [Ca 2+] and [PO43-] levels on the formation of calcium phosphate conversion coatings on die-cast magnesium alloy AZ91D

Corros. Sci., 55 (2012), pp. 226-232, 10.1016/j.corsci.2011.10.022

[34] C.Y. Zhang, S.J. Liao, B.X. Yu, X.P. Lu, X.B. Chen, T. Zhang, F.H. Wang

Ratio of total acidity to pH value of coating bath: a new strategy towards phosphate conversion coatings with optimized corrosion resistance for magnesium alloys
Corros. Sci. (2019), 10.1016/j.corsci.2019.01.046

[35] M.S. Song, R.C. Zeng, Y.F. Ding, R.W. Li, M. Easton, I. Cole, N. Birbilis, X.B. Chen
Recent advances in biodegradation controls over Mg alloys for bone fracture management: a review
J. Mater. Sci. Technol. (2019), 10.1016/j.jmst.2018.10.008

[36] I.A. Standard
ASTM C633 − 13: Standard Test Method for Adhesion or Cohesion Strength of Thermal Spray Coatings
(2001), 10.1520/C0633-13.Copyright

[37] A.I. 10993-5:2009
Biological Evaluation of Medical Devices — Part 5: Tests for In Vitro Cytotoxicity
(2002)

[38] J.H. Hanks
Hanks' balanced salt solution and pH control
Methods Cell Sci, Springer (1975)

http://www.springerlink.com/index/P214662317R6810J.pdf

[39] R.S. Stampella, R.P.M. Procter, V. Ashworth
Environmentally-induced cracking of magnesium
Corros. Sci. (1984), 10.1016/0010-938X(84)90017-9

[40] G. Song, D. StJohn
The effect of zirconium grain refinement on the corrosion behaviour of magnesium-rare earth alloy MEZ
J. Light. Met. (2002), 10.1016/S1471-5317(02)00008-1

[41] M.E. Orazem, B. Tribollet
Electrochemical Impedance Spectroscopy

(2008), 10.1002/9780470381588

[42] H. Fricke XXXIII. The theory of electrolytic polarization, London, Edinburgh, Dublin Philos. Mag. J. Sci. (1932). doi:https://doi.org/10.1080/14786443209462064.

[43] G.J. Brug, A.L.G. van den Eeden, M. Sluyters-Rehbach, J.H. Sluyters

The analysis of electrode impedances complicated by the presence of a constant phase element

J. Electroanal. Chem., 176 (1984), pp. 275-295, 10.1016/S0022-0728(84)80324-1

[44] L. Nyikos, T. Pajkossy

Fractal dimension and fractional power frequency-dependent impedance of blocking electrodes

Electrochim. Acta (1985), 10.1016/0013-4686(85)80016-5

[45] B. Sapoval

Linear and non-linear behavior of fractal and irregular electrodes

Solid State Ionics (1995), 10.1016/0167-2738(94)00171-N

[46] P. Delahay Ed, C.W. Tobias Ed

Advances in Electrochemistry and Electrochemical Engineering, V 7, Electrochemistry

Intersci. Publ, Div John Wiley Sons, Inc (1970), 10.1016/s0003-2670(01)80292-0

[47] R. De Levie

Electrochemical response of porous and rough electrodes

Adv. Electrochem. Electrochem. Eng., 6 (1967), pp. 329-397

[48] J. Vogelsang, W. Strunz

The evaluation of experimental dielectric data of barrier coatings by means of different models

Electrochim. Acta (2001), 10.1016/S0013-4686(01)00644-2

[49] J.B. Jorcin, M.E. Orazem, N. Pébère, B. Tribollet

CPE analysis by local electrochemical impedance spectroscopy

Electrochim. Acta (2006), 10.1016/j.electacta.2005.02.128

[50] J. Newman

Current distribution on a rotating disk below the limiting current

J. Electrochem. Soc. (1966), 10.1149/1.2423795

[51] M.E. Orazem, P. Agarwal, L.H. Garcia-Rubio

Critical issues associated with interpretation of impedance spectra

J. Electroanal. Chem. (1994), 10.1016/0022-0728(94)87056-X

[52] M. Durbha

A mathematical model for the radially dependent impedance of a rotating disk electrode

J. Electrochem. Soc. (1999), 10.1149/1.1391914

[53] P. Zoltowski

On the electrical capacitance of interfaces exhibiting constant phase element behaviour

J. Electroanal. Chem. (1998), 10.1016/S0022-0728(97)00490-7

[54] V. Shkirskiy, A.D. King, O. Gharbi, P. Volovitch, J.R. Scully, K. Ogle, N. Birbilis

Revisiting the electrochemical impedance spectroscopy of magnesium with online inductively coupled plasma atomic emission spectroscopy

ChemPhysChem (2015), 10.1002/cphc.201402666

[55] Esmaily, J.E. Svensson, S. Fajardo, N. Birbilis, G.S. Frankel, S. Virtanen, R. Arrabal, S. Th omas, L.G. Johansson

Fundamentals and advances in magnesium alloy corrosion

Prog. Mater. Sci. (2017), 10.1016/j.pmatsci.2017.04.011

[56] G. Song, A. Atrens, D.St. John, X. Wu, J. Nairn

The anodic dissolution of magnesium in chloride and sulphate solutions

Corros. Sci. (1997), 10.1016/S0010-938X(97)00090-5

[57] G. Baril, G. Galicia, C. Deslouis, N. Pébère, B. Tribollet, V. Vivier

An impedance investigation of the mechanism of pure magnesium corrosion in sodium sulfate solutions

J. Electrochem. Soc. (2007), 10.1149/1.2401056

[58] N. Pebere, C. Riera, F. Dabosi

Investigation of magnesium corrosion in aerated sodium sulfate solution by electrochemical impedance spectroscopy

Electrochim. Acta (1990), 10.1016/0013-4686(90)87043-2

[59] Y. Shao, H. Huang, T. Zhang, G. Meng, F. Wang

Corrosion protection of Mg-5Li alloy with epoxy coatings containing polyaniline

Corros. Sci., 51 (2009), pp. 2906-2915, 10.1016/j.corsci.2009.08.012

[60] G. Baril, N. Pébère

Corrosion of pure magnesium in aerated and deaerated sodium sulphate solutions

Corros. Sci. (2001), 10.1016/S0010-938X(00)00095-0

[61] J.W. Turrentine

Reversed electrolysis

J. Phys. Chem. (1908), 10.1021/j150096a006

[62] R.L. Petty, A.W. Davidson, J. Kleinberg

The anodic oxidation of magnesium metal: evidence for the existence of unipositive magnesium

J. Am. Chem. Soc. (1954), 10.1021/ja01631a013

[63] W. Beetz

XXXIV. On the development of hydrogen from the anode

London, Edinburgh, Dublin Philos. Mag. J. Sci. (1866), 10.1080/14786446608644179

[64] G.S. Frankel, A. Samaniego, N. Birbilis

Evolution of hydrogen at dissolving magnesium surfaces

Corros. Sci., 70 (2013), pp. 104-111, 10.1016/j.corsci.2013.01.017

[65] A. Atrens, G.L. Song, M. Liu, Z. Shi, F. Cao, M.S. Dargusch

Review of recent developments in the field of magnesium corrosion

Adv. Eng. Mater., 17 (2015), pp. 400-453, 10.1002/adem.201400434

[66] G.L. Song, A. Atrens

Corrosion mechanisms of magnesium alloys

Adv. Eng. Mater., 1 (1999), pp. 11-33, 10.1002/(SICI)1527-2648(199909)1:1<11::AID-ADEM11>3.0.CO;2-N

[67] A. Atrens, W. Dietzel

The negative difference effect and unipositive Mg

Adv. Eng. Mater., 9 (2007), pp. 292-297, 10.1007/s00170-016-8694-1

[68] S. Thomas, N.V. Medhekar, G.S. Frankel, N. Birbilis

Corrosion mechanism and hydrogen evolution on Mg

Curr. Opin. Solid State Mater. Sci. (2015), 10.1016/j.cossms.2014.09.005

[69] G.Y. Li, J.S. Lian, L.Y. Niu, Z.H. Jiang, Q. Jiang

Growth of zinc phosphate coatings on AZ91D magnesium alloy

Surf. Coatings Technol., 201 (2006), pp. 1814-1820, 10.1016/j.surfcoat.2006.03.006

[70] A.P. Miller

Lange's handbook of chemistry

Am. J. Public Heal. Nations Heal. (2008), 10.2105/ajph.31.12.1324-a

[71] P. Delahay, C.W. Tobias

Advances in Electrochemistry and Electrochemical Engineering

Wiley (1967)

[72] R. de Levie

On porous electrodes in electrolyte solutions-IV

Electrochim. Acta (1964), 10.1016/0013-4686(64)85015-5

[73] F. Mansfeld

Use of electrochemical impedance spectroscopy for the study of corrosion protection by polymer coatings

J. Appl. Electrochem. (1995), 10.1007/BF00262955

[75] L. Jianguo, G. Gaoping, Y. Chuanwei

EIS study of corrosion behaviour of organic coating/Dacromet composite systems

Electrochim. Acta (2005), 10.1016/j.electacta.2004.12.010

[76] W. Zai, M.H. Wong, H.C. Man

Improving the wear and corrosion resistance of CoCrMo-UHMWPE articulating surfaces in the presence of an electrolyte

Appl. Surf. Sci., 464 (2019), pp. 404-411, 10.1016/j.apsusc.2018.09.027

[77] C. Hamanishi, K. Kitamoto, S. Tanaka, M. Otsuka, Y. Doi, T. Kitahashi

A self-setting TTCP-DCPD apatite cement for release of vancomycin

J. Biomed. Mater. Res. (1996), 10.1002/(SICI)1097-4636(199623)33:3<139::AID-JB3>3.0.CO;2-R

[78] R.Z. LeGeros

Calcium phosphate-based osteoinductive materials

Chem. Rev. (2008), 10.1021/cr800427g